

Long-term retention of antigens in germinal centers is controlled by the spatial organization of the follicular dendritic cell network

Received: 18 August 2022

Accepted: 13 June 2023

Published online: 13 July 2023

 Check for updates

Ana Martínez-Riaño^{1,2}, Shenshen Wang³, Stefan Boeing⁴, Sophie Minoughan¹, Antonio Casal¹, Katelyn M. Spillane¹, Burkhard Ludewig¹& Pavel Tolar^{1,2}

Germinal centers (GCs) require sustained availability of antigens to promote antibody affinity maturation against pathogens and vaccines. A key source of antigens for GC B cells are immune complexes (ICs) displayed on follicular dendritic cells (FDCs). Here we show that FDC spatial organization regulates antigen dynamics in the GC. We identify heterogeneity within the FDC network. While the entire light zone (LZ) FDC network captures ICs initially, only the central cells of the network function as the antigen reservoir, where different antigens arriving from subsequent immunizations colocalize. Mechanistically, central LZ FDCs constitutively express subtly higher CR2 membrane densities than peripheral LZ FDCs, which strongly increases the IC retention half-life. Even though repeated immunizations gradually saturate central FDCs, B cell responses remain efficient because new antigens partially displace old ones. These results reveal the principles shaping antigen display on FDCs during the GC reaction.

The generation of high-affinity antibodies that neutralize pathogens is a hallmark of the humoral response. The response is initiated by the binding of antigens to antigen-specific B cells in the follicles of secondary lymphoid organs. Activated B cells generate an initial burst of plasma and memory cells and also seed GCs, where they further diversify their B cell receptor (BCR) repertoire and undergo selection for antigen affinity¹. B cells with higher affinity BCRs outcompete B cells with lower affinity thanks to the survival and proliferative advantage instigated by higher BCR binding to antigens and higher T cell help^{2,3}. This selection takes several weeks and increases the affinity of antibodies produced by GC-generated plasma cells (PCs). Thus, a constant

supply of antigens to GC B cells is essential to fuel affinity maturation, critical for antibody-mediated protection.

Although secondary lymphoid organs are constantly exposed to antigens in lymph or blood, the entry of antigens into B cell follicles is restricted^{4,5} and their retention require binding to FDCs^{6–8}. FDCs are stromal cells that develop from perivascular or subcapsular precursors of the spleen and lymph node (LN), respectively^{9,10}, in response to LT α 1 β 2 and tumor necrosis factor (TNF) produced by B cells^{11–14}. FDCs form tight networks throughout the follicle via long intermingled dendrites and produce factors that control B cell survival, localization and elimination upon apoptosis (for example, CXCL13 (ref. 15), GGT5

¹Immune Receptor Activation Laboratory, The Francis Crick Institute, London, UK. ²Division of Infection and Immunity, Institute of Immunity and Transplantation, University College London, London, UK. ³Department of Physics and Astronomy, University of California Los Angeles, Los Angeles, CA, USA. ⁴Bioinformatics and Biostatistics Science Technology Platform, The Francis Crick Institute, London, UK. ⁵Department of Physics, King's College London, London, UK. ⁶Randall Centre for Cell and Molecular Biophysics, King's College London, London, UK. ⁷Institute of Immunobiology, Medical Research Center, Kantonsspital St. Gallen, St. Gallen, Switzerland.  e-mail: p.tolar@ucl.ac.uk

(ref. 16), TNFSF13B (BAFF)¹⁷ and MFGE8 (ref. 18)). Within the first day after immunization, complement-coated antigens are shuttled to FDCs by noncognate B cells from the subcapsular sinus of the LN or from the marginal zone of the spleen^{19,20}. Subsequently, FDCs retain and display the intact antigens for several weeks. A related subset termed dark zone (DZ) FDC (also called *Cxcl12*-expressing reticular cells) does not retain antigens but organizes the GC DZ by producing CXCL12 (refs. 6,21).

Canonical (also termed LZ) FDCs capture antigens in complement-coated particles or immune complexes (ICs) via two complement receptors, CR1 (CD35) and CR2 (CD21), which bind to the complement fragment C3d covalently attached to the antigen. In the mouse, both receptors are encoded by a single *C2* gene and, therefore, we refer to them both as CR2 here. In addition, a subpopulation of activated FDCs in the GC expresses an array of Fc-receptors (FCGR2B, FCER2A and FCMAR)²², whose roles in antigen retention are less clear, but may fine-tune B cell selection^{23–26}.

In line with the ability of FDCs to retain antigens, the deletion of CR2 from stromal cells reduces antibody responses to primary and secondary immunization^{27,28}. However, some studies did not find a role for FDC antigen retention in the GC response²⁹. Nevertheless, enhancing the deposition of antigens on FDCs leads to augmented GC responses and the production of highly evolved antibody specificities, suggesting that targeting antigens to FDCs may be beneficial in vaccine-induced protection^{30–32}.

To better understand the long-term dynamics of antigen retention in B cell follicles and their replacement upon reimmunization, we imaged clarified LNs from mice immunized with fluorescent ICs. We observed striking changes in antigen localization over time: while the entire FDC network captured antigen initially, only the central cells retained antigen throughout the duration of the GC and served as long-term antigen reservoirs. This pattern was independent of the GC itself. Single-cell transcriptomics corroborated functional heterogeneity within LZ FDCs. Mechanistically, central FDCs had slower IC dissociation due to subtly higher levels of CR2 on their surfaces. Repeated immunizations partially saturated the central FDCs, but also replaced previous antigens, suggesting a dynamic competition of ICs for CR2. Antigen replacement on central FDCs, together with nonsaturable antigen capture by peripheral FDCs, may underlie the efficient B cell response to repeated challenges. Understanding the basis of antigen dynamics on the FDC network will guide the generation of more efficient vaccines aiming to improve antigen retention in the GC.

Results

Long-term antigen retention is mediated by central FDCs

To study the retention of vaccine antigens during the GC response, we immunized mice with fluorescent antigen IC, known to efficiently bind to FDCs¹⁹, and imaged clarified draining LN at different timepoints postinjection using three-dimensional confocal microscopy (Fig. 1a). We observed that, 24 h postimmunization, most of the antigen was loaded onto the entire FDC network of each B cell follicle. However,

on days 7 and 14 after immunization, when GCs form, the antigen localization became restricted to the center of each follicle (Fig. 1b and Extended Data Fig. 1a). To quantify the distribution of the antigen over time, we divided each FDC network into five concentric shells and calculated the ratio of antigen to anti-CR2 fluorescence (Extended Data Fig. 1b). The quantification confirmed that on day 1 postimmunization, antigen was distributed equally across the FDC networks, while on days 7 and 14 after immunization, it was located preferentially in the center (Fig. 1c). This antigen centralization was independent of the presence of the alum adjuvant during immunization (Fig. 1c,d). Thus, antigen localization is dynamic during the onset of the GC.

To understand whether subsequent immunizations generate a similar pattern of antigen distribution, we followed the first immunization (IC-Phycoerythrin, IC-PE) 6 days later with a second immunization with a different antigen-IC (IC-488; Fig. 1e,f and Extended Data Fig. 1c,d). Imaging of clarified LNs showed that, 24 h after the second immunization, the second antigen-IC was present over the entire FDC network, while the first antigen was already localized in the center. Seven days later, the second antigen also centralized and colocalized with the first antigen on the central FDCs. Thus, while the entire FDC network captures incoming ICs initially, the retention of the antigens takes place exclusively on the central FDCs of the network, independently of the presence of previous antigens.

We observed antigen retention on central FDCs up to 56 days postimmunization (Extended Data Fig. 1e). On day 21, the centralized antigen colocalized with GCs (Extended Data Fig. 1f). Similar localization of antigens on central FDCs was observed 7 days after immunization with human immunodeficiency virus (HIV)-gp120 nanoparticles (Extended Data Fig. 1g), which trigger complement activation independently of IC formation²⁴. Furthermore, flow cytometry showed that the percentage of FDCs loaded with antigen-IC decreased from day 1 to day 14 postimmunization (Extended Data Fig. 1h,g). Altogether, these data suggest a heterogeneity within the FDC network, with the periphery capturing antigens transiently and the center retaining antigens beyond the first week postimmunization.

Dynamics of antigen retention are independent of the GC

Changes in antigen localization may be driven by the reorganization of the FDC network after immunization. In agreement with previous data¹⁰, we observed that IC immunization increased the number of FDCs and the volume of FDC networks (Fig. 2a and Extended Data Fig. 2a). GC B cells (GL7⁺ Bcl6⁺) and T follicular helper cells (PD1⁺ Bcl6⁺) colocalized with both the central and peripheral FDCs, although some peripheral FDCs extended beyond the GC (Extended Data Fig. 2b).

To understand whether B cell activation promotes changes in the FDC network after immunization, we analyzed mice expressing transgenic BCRs specific for noncognate antigens, B1-8ⁿ (B1-8ⁿ Igκ^{-/-}, BCR specific for NP hapten) or MD4 (BCR specific for hen egg lysozyme) (Methods). Both BCR transgenic mice had very few FDCs that formed poorly organized networks and were deficient in antigen capture at

Fig. 1 | Long-term dynamics of antigen localization in B cell follicles.

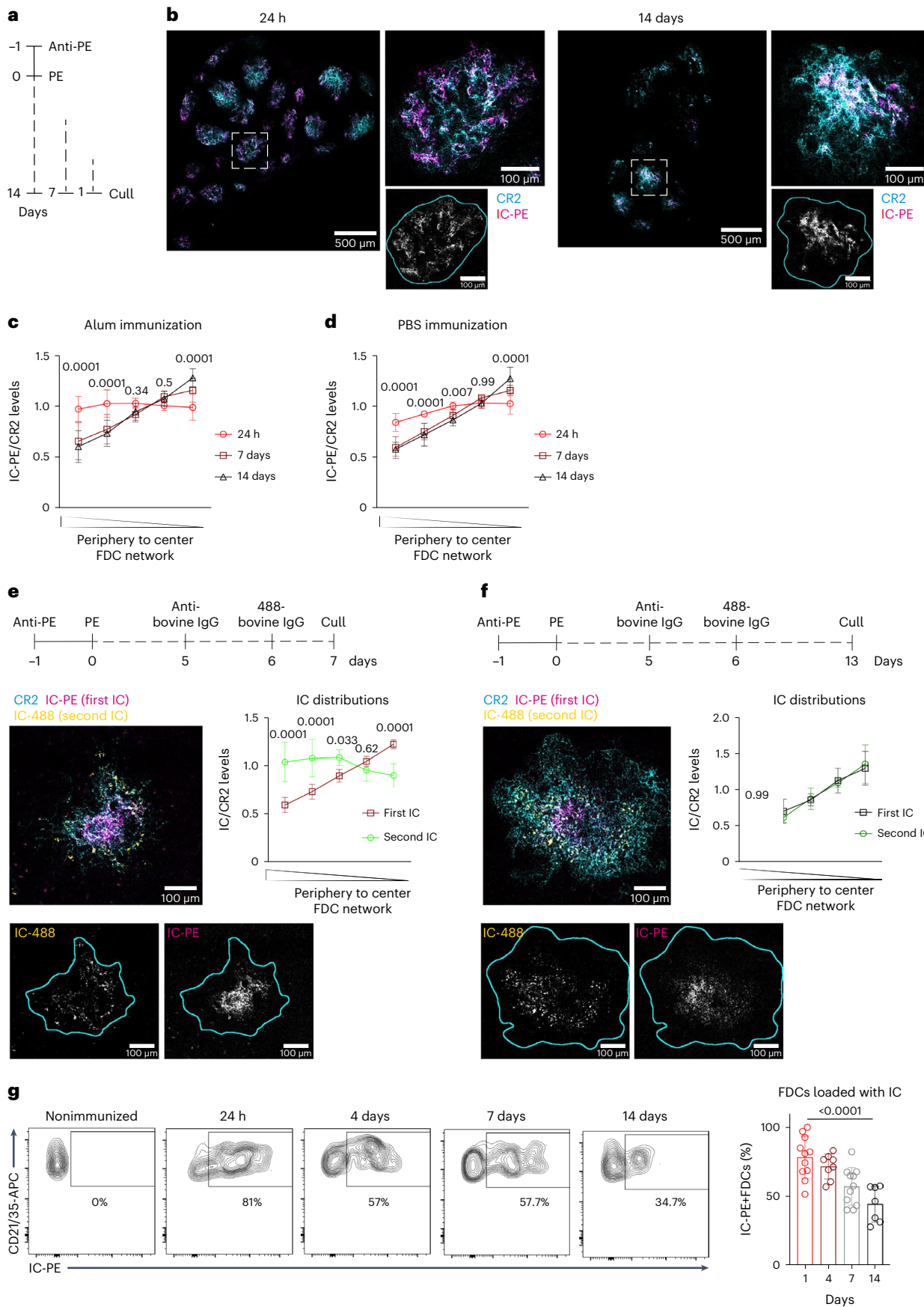
a, Immunization workflow to analyze IC-PE localization in draining LNs after 24 h and after 7 and 14 days. IC-PE immunization is performed by injecting PE-specific antibody (anti-PE) i.p. followed by PE subcutaneously the day after.

b, Representative confocal section of clarified draining LNs 24 h (left) and 14 days (right) after immunization with IC-PE (magenta). FDC networks are stained by anti-CD21/35 antibody binding to CR2 on FDCs (cyan). White squares indicate the region magnified. Single-color image of IC-PE is shown in gray. Cyan line demarcates the FDC network boundary based on anti-CD21/35 staining.

c, Quantification of antigen distribution on the FDC networks of mice immunized with IC-PE for 24 h ($n = 6$), 7 days ($n = 8$) and 14 days ($n = 9$) with antigen embedded in alum. Quantification workflow is described in Extended Data Fig. 1a (three experiments). **d**, Antigen distribution on the FDC network of mice immunized as described in **c** with antigen diluted in PBS ($n = 6$ and 7 mice; two experiments).

e, Distribution of ICs on the FDC network after a repeated immunization. LNs were analyzed 7 days after the first IC injection (IC-PE) and 24 h after the second one (IC-488). A representative confocal image of an FDC network (anti-CD21/35 in cyan; IC-PE in magenta; IC-488 in yellow) with single-color images of IC-488 (left) and IC-PE (right) shown below. Cyan line demarcates the FDC network boundary based on anti-CD21/35 staining. Quantification of the distribution of both ICs in the FDC network is shown in the graph ($n = 6$ mice; two experiments).

f, Distribution of ICs on the FDC network 7 days after the repeated immunization (IC-488, second IC) ($n = 5$ mice) and 14 days (IC-PE, first IC) ($n = 7$ mice) after the first immunization as described in **e** (two experiments). **g**, Flow cytometry plots and quantification of the percentage of IC-PE⁺ FDCs at different timepoints after IC-PE immunization ($n = 7, 8$ and 11 mice). All quantitative data show means \pm s.d. and analysis by two-tailed two-way analysis of variance (ANOVA) with multiple comparisons.



24 h postimmunization with IC (Extended Data Fig. 2c,d). Thus, the basal level of BCR-driven B cell activation is necessary to promote the development of a well-organized FDC network, preventing a more detailed analysis of antigen dynamics.

To test the role of T cell-dependent B cell activation and GC formation, we blocked CD40 signaling by anti-CD40L blocking antibody injected after immunization³³ (Fig. 2b). Compared with isotype control, the anti-CD40L antibody completely blocked the GC reaction (Extended Data Fig. 2e) and the expansion of FDCs induced upon immunization (Fig. 2c). However, the anti-CD40L antibody did not affect antigen distribution on day 14 (Fig. 2d). In addition, the anti-CD40L treated mice had a similar percentage of FDCs loaded with either the first or the second IC compared with the control group (Fig. 2e), and their FDCs retained similar amounts of the second antigen 7 days postinjection, while containing only slightly less of the first IC 14 days postinjection (Fig. 2f). Thus, CD40L-dependent signals promote FDC expansion after immunization, but are not involved in antigen centralization or retention for up to 7 days, although they may contribute at later timepoints.

Heterogeneity in LZ FDCs orchestrates antigen retention

To explore the differences between the peripheral and central FDCs, we took advantage of sequential immunizations on days 0 and 6 with two differently labeled antigens (Fig. 3a). One day after the last immunization, central FDCs contain both antigens while peripheral FDCs contain only the last, allowing us to distinguish both populations by flow cytometry (Fig. 3b). Central FDCs expressed higher levels of FCGR2B, FCER2A (Fig. 3c) and CR2 than peripheral FDCs (Fig. 3d) but had similar levels of podoplanin (PDPN) (Fig. 3e). Similar observations were made when comparing FDCs that retained antigen at day 7 with those that did not (Extended Data Fig. 3a).

Recently, single-cell transcriptomics revealed two subsets of FDCs: the LZ FDCs located in a peripheral area closer to the subcapsular sinus and DZ FDCs closer to the T cell zone^{6,21}. LZ FDCs can be distinguished by high expression of CR2, and myosin heavy chain 11 (MYH11), whereas DZ FDCs express CXCL12 and PDLIM3 (refs. 6,21). To understand how the central and peripheral FDCs relate to LZ and DZ FDC subsets, we analyzed the expression of MYH11 (ref. 6). Both central and peripheral FDCs expressed high levels of MYH11, indicating that both populations belong to LZ FDCs (Extended Data Fig. 3b).

To understand better the heterogeneity within the FDCs, we performed scRNASeq of the B follicle reticular cells marked by CXCL13-Cre TdTomato⁶. Mice were analyzed at two different timepoints after immunization with antigen-IC (Extended Data Fig. 4a); however, we performed all analyses on pooled samples, as we did not observe differences in gene expression between timepoints. Unsupervised clustering revealed ten distinct clusters of cells. Two corresponded to contaminating hematopoietic cells identified by their lack of *Cxcl13* expression and high expression of *H2-Aa* (Extended Data Fig. 4b). The other eight clusters corresponded to follicular stromal cells, of which seven were similar to clusters previously described using similar approaches^{6,7} (Fig. 4a). Assignment of these seven clusters using subset-specific

genes identified two clusters of FDCs sharing *Cr2* expression; MRCs expressing *Madcam1* and *Tnfsf11*; IFRCs showing *Tnfsf11* and *Ch25h* expression; TBRCs with the expression of *Fmod* and *Ccl21a*; and two clusters of MedRCs sharing *Nr4a1* expression. The eighth cluster corresponded to follicular stromal cells with a prominent interferon-related signature, which could correspond to an activated stromal subset.

Further analysis of the two FDC clusters indicated heterogeneity within the FDC 1 cluster, with only a fraction of cells expressing *Fcgr2b*, *Fcer2a* and *Cd200*. In contrast, these genes were expressed homogenously in FDC cluster 2 (Fig. 4b). Furthermore, the cells in FDC cluster 1 that did not express these genes expressed higher levels of *Cxcl12* (Extended Data Fig. 4b). Consequently, we decided to re-embed FDC 1 and 2 cells and perform subclustering, which grouped the cells into three FDC clusters (Fig. 4c). We assigned one cluster to DZ FDCs based on the low *Cr2* and high *Pdlim3* expression, and two clusters to LZ FDCs based on their high *Cr2* and *Myh11* expression (LZ 1 and LZ 2) (Fig. 4d and Extended Data Fig. 4c). Even though the differences in *Pdlim3* and *Myh11* expression between clusters were not significant because of the low number of cells, the combination of *Pdlim3*, *Myh11* and *Cr2* allowed us to discriminate the three populations. LZ 1 cluster expressed lower levels of *Fcgr2b* and *Fcer2a*, relating this population to peripheral FDCs, while LZ 2 cluster expressed higher levels of *Fcgr2b* and *Fcer2a*, relating them to the central FDC (Extended Data Fig. 4c and Figs. 3c and 4d). To confirm the relationship of the LZ 1 and LZ 2 clusters to peripheral and central FDCs in situ, we stained clarified LN 7 days after IC-PE immunization with antibodies specific for FCGR2B. Images showed that central FDCs that retained antigen colocalized with the brightest FCGR2B-expressing cells, indicating that the LZ 2 cluster corresponds to central FDCs (Extended Data Fig. 4d).

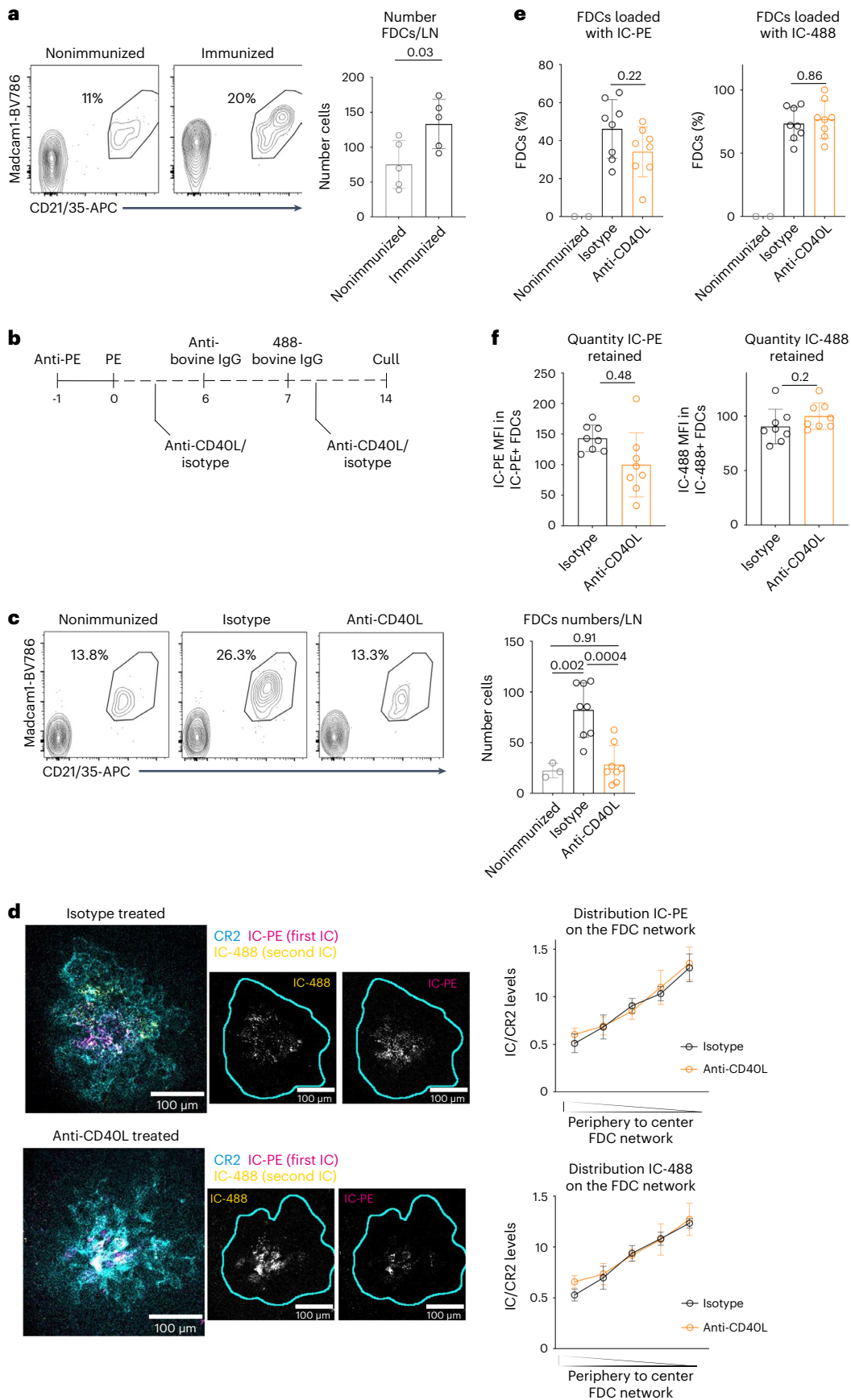
Analysis of the pathways enriched among differentially expressed genes using STRING³⁴ (Fig. 4e) showed that central LZ 2 FDCs upregulated molecules related to antigen presentation to B cells, but also to T cells, such as major histocompatibility complex class I (MHC-I) and MHC-II related genes, together with several subunits of the proteasome complex. An increase in MHC-I expression on central versus peripheral FDCs was also observed at the protein level by flow cytometry (Fig. 4f). Central LZ FDCs also upregulated expression of genes involved in the mitochondrial respiratory complex participating in oxidative phosphorylation and genes controlling cytoskeleton organization, which could explain their high degree of dendritic organization and compaction. On the other hand, peripheral LZ FDCs seemed more responsive to extracellular signals, with the upregulation of different cytokine receptor genes and intermediaries of MAPK and TNF signaling pathways (Fig. 4e). These results suggest that two populations exist within LZ FDCs, likely corresponding to the central and peripheral FDCs identified by imaging.

Both peripheral and central FDC show low antigen degradation

To understand the mechanisms underlying the selective retention of antigens by central FDCs, we compared the ability of FDC populations

Fig. 2 | CD40L signals induce FDC network expansion and activation but do not regulate antigen centralization or retention. **a**, Flow cytometry plots gated on FDCs as shown in Extended Data Fig. 1h and numbers of FDCs in LNs of nonimmunized mice and mice immunized with IC-PE 13 days prior to analysis ($n = 5$ mice). **b**, Experimental workflow to analyze the effect of CD40 signaling on antigen retention by FDCs. Mice were immunized first with IC-PE and then treated with anti-CD40L or isotype control antibodies (200 μ g per mouse; two subsequent days). Seven days after the first immunization, mice were injected with the second IC (IC-bovine-488) and treated again with anti-CD40L or isotype control. Draining LNs were analyzed 7 days after the second immunization. **c**, Flow cytometry plots and numbers of FDCs in nonimmunized mice (gray; $n = 3$ mice) or mice immunized and treated with either anti-CD40L antibody (orange; $n = 8$ mice) or isotype control (black; $n = 8$ mice) as described in **b**

(two experiments). **d**, Confocal images and quantification of the ICs distribution in mice treated as described in **b**. Single-color images (gray) show the localization of IC-PE and IC-488. Cyan line demarcates the FDC network boundary. Upper graph shows the distribution of the first antigen (14 days postinjection). Lower graph shows the distribution of the second (7 days postinjection) ($n = 8$ LNs from four mice). **e**, Quantification of the percentage of FDCs loaded with IC-PE (first IC, left graph) and IC-488 (second IC, right graph) in nonimmunized ($n = 3$) or immunized and anti-CD40L ($n = 8$) or isotype control-treated ($n = 8$) mice as described in **b**. **f**, Quantity of ICs retained by FDCs measured as mean fluorescent intensity (MFI) in mice treated with anti-CD40L or isotype control antibodies ($n = 8$ mice). All quantitative data show means \pm s.d. and analyses by two-tailed *t*-test or one-way ANOVA with multiple comparisons.



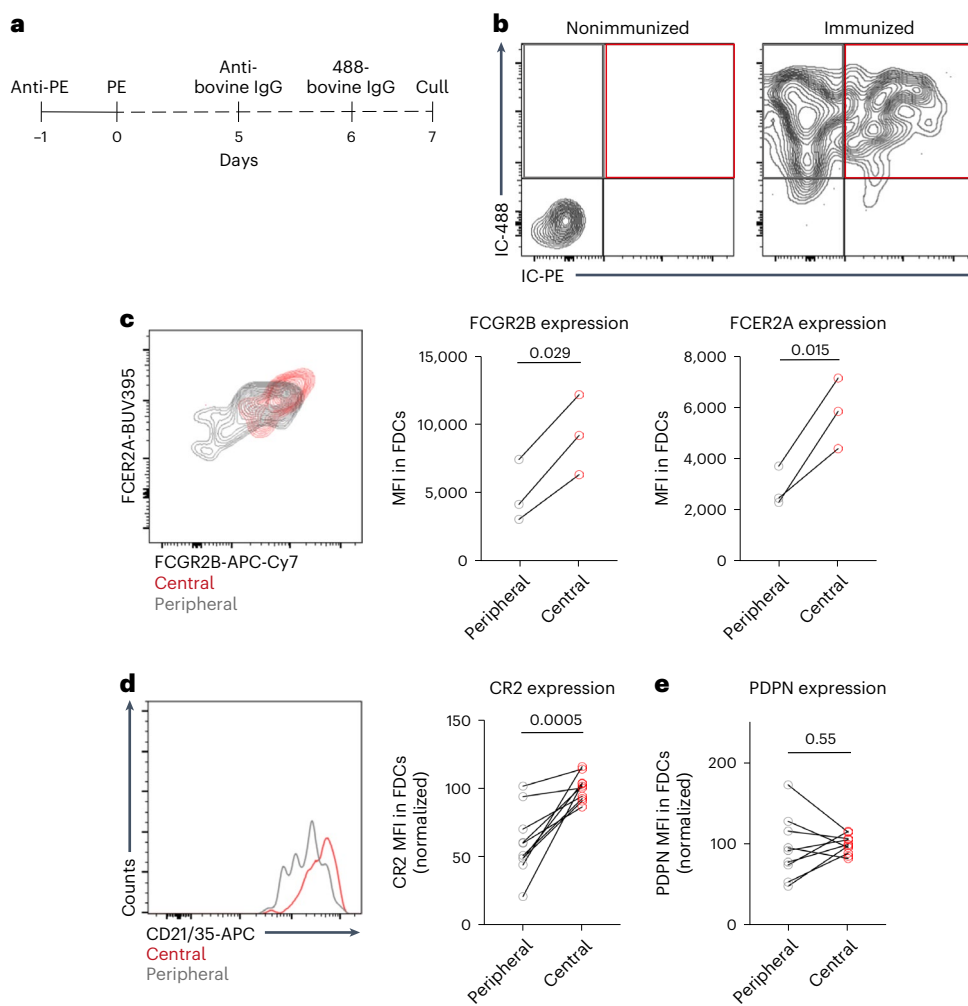


Fig. 3 | Central and peripheral LZ FDCs express different levels of IC-binding receptors. **a**, Immunization workflow to distinguish peripheral and central FDCs by flow cytometry. Mice were immunized first with IC-PE, followed by IC-488 6 days later. LN were analyzed 24 h after the second immunization. **b**, Flow cytometry gating strategy to identify peripheral (gray gate) and central (red gate) FDCs in LNs of immunized mice following workflow described in **a**. Retention of the first IC (IC-PE) distinguishes central (IC-PE⁺ IC-488⁺, red gate)

from peripheral FDCs (IC-PE⁺ IC-488⁻, gray gate). **c**, FCGR2B (stained with anti-CD16/32 antibodies) and FCER2A (stained with anti-CD23 antibodies) membrane expression on central (red) and peripheral (gray) FDCs from mice immunized as described in **a** and **b** ($n = 3$ mice). **d**, CR2 membrane expression on FDCs as described in **a** and **b** ($n = 10$ mice, three experiments). **e**, PDPN membrane expression on FDCs as described in **a** and **b** ($n = 10$ mice, three experiments). *P* values are from a two-tailed paired *t*-test.

to keep antigens in their native conformation. We generated an antigen-degradation sensor by labeling an antigen (bovine IgG) with Atto488 and its quencher (BHQ-1), along with a nonquenchable dye AF647 (Fig. 5a). Atto488 fluorescence was efficiently quenched, but recovered after proteolysis (Extended Data Fig. 5a). We conjugated the sensor to anti-IgM-coated beads, which can be phagocytosed and processed by B cells³⁵. After incubation with B cells, the percentage of B cells containing quenched antigen (Atto488-low cells) decreased over time (Extended Data Fig. 5b), while the total antigen degradation increased compared with beads containing a control sensor lacking the quencher. Thus, the sensor detects physiological levels of antigen degradation.

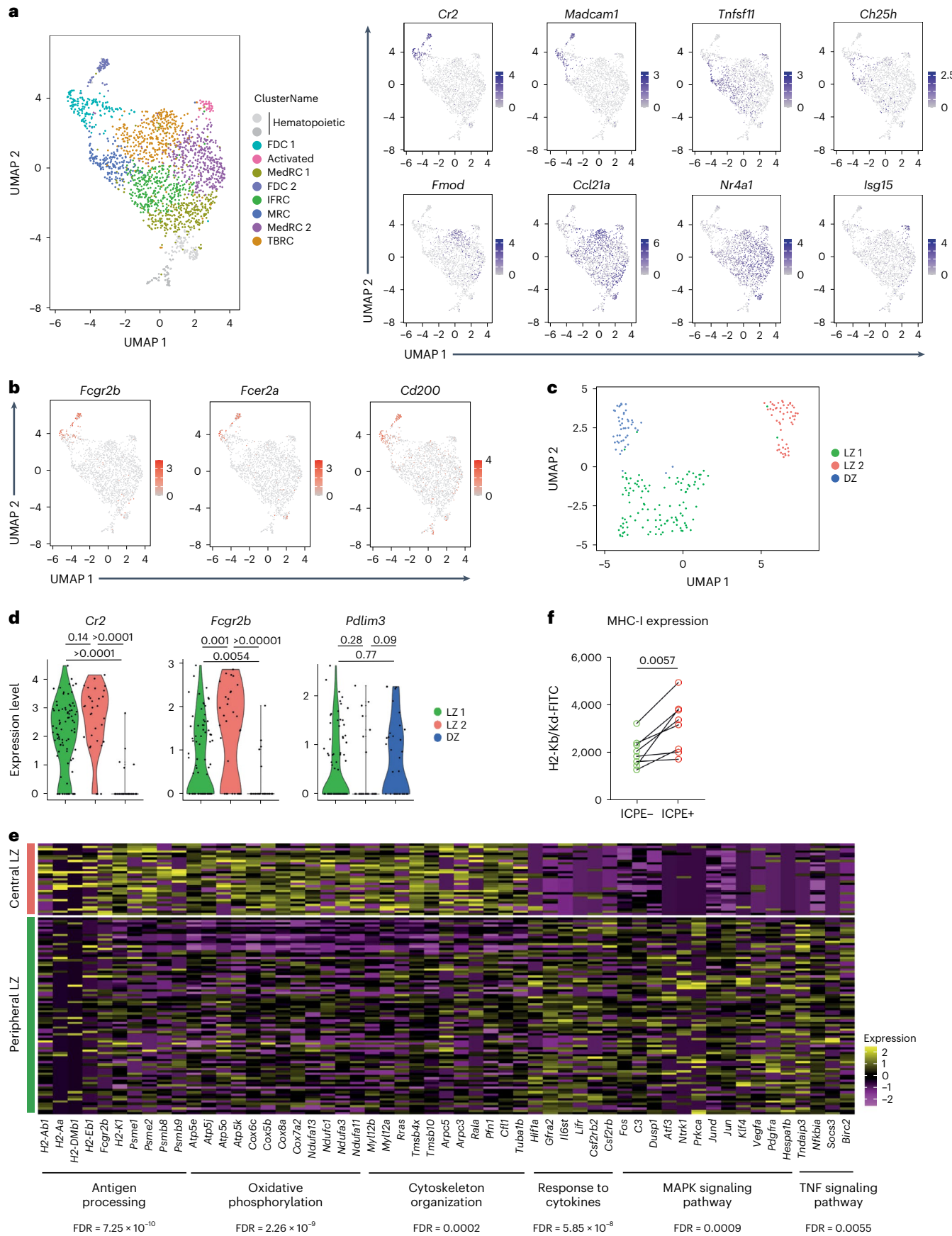
To measure antigen degradation by FDCs *in vivo*, mice were first immunized with IC-PE to differentiate central and peripheral FDCs and, 7 days later, immunized with the antigen-degradation sensor IC. LN cells were analyzed at 24 h, 3 days and 4 days (Fig. 5b). As expected, FDCs showed lower antigen degradation compared with B cells (Extended Data Fig. 5c,d). However, IC-PE-positive central and IC-PE-negative peripheral FDCs showed similar sensor degradation (Fig. 5c), indicating that the loss of antigen in the periphery of the FDC network is not caused by increased antigen degradation.

CR2 density controls antigen retention

Central FDCs may retain antigens better due to the lower dissociation of ICs from their surfaces. This could involve the enhanced expression of FCGR2B on central FDCs after immunization. However, enhanced expression of FCGR2B required CD40L-induced signaling (Extended Data Fig. 6a), whereas ICs retention did not (Fig. 2d–f), making a contribution from FCGR2B unlikely.

In contrast, localized antigen retention could involve enhanced surface levels of CR2 on central FDCs (Fig. 3d and Extended Data Fig. 3a), which were independent of immunization or CD40L blockade (Extended Data Fig. 6a). We confirmed that central FDCs express more CR2 than peripheral FDCs at the steady-state by analyzing CR2 expression in clarified LNs from nonimmunized mice by microscopy and normalizing to PDPN (Fig. 6a), which was similarly expressed on all FDCs (Fig. 3e).

To validate that the retention of antigen-ICs by FDCs was CR2-mediated, lethally irradiated CD45.2⁺ WT and *Cr2* knock-out (KO) mice were bone marrow reconstituted with CD45.1/2 wild-type (WT) haematopoietic cells and immunized with two subsequent antigen-ICs (Extended Data Fig. 6b). Since stromal cells are radioresistant, bone



Antigen processing FDR = 7.25×10^{-10}

Oxidative phosphorylation FDR = 2.26×10^{-9}

Cytoskeleton organization FDR = 0.0002

Response to cytokines FDR = 5.85×10^{-8}

MAPK signaling pathway FDR = 0.0009

TNF signaling pathway FDR = 0.0055

Fig. 4 | Single-cell transcriptomics differentiates two LZ FDC clusters with different functional activity. **a**, Uniform manifold approximation and projection (UMAP) plot of Cxcl13-TdTomato expressing LN stromal cells. Left panel shows the merged data from mice immunized as described in Extended Data Fig. 4a. Right panels show feature plots illustrating the expression of subset-specific marker genes for the indicated LN stromal cell clusters (data pooled from three experiments, six to seven mice per experiment). **b**, Feature plots showing the expression pattern of *Fcgr2b*, *Fcer2a* and *Cd200*. **c**, UMAP of FDC1 and FDC2 cells from **a** after subclustering. **d**, Violin plots showing the expression of marker

genes specific for the three FDC clusters (LZ 1 in green, LZ 2 in red and DZ in blue). One-tail adjusted *P* for multiple comparisons. **e**, Heatmap of scaled expression of genes differentially expressed (greater than twofold increased expression; adjusted *P* < 0.05) between LZ 1 and LZ 2 FDC subsets grouped into functional and signaling pathways identified by STRING (one-tail false discovery rate (FDR) for multiple comparisons < 0.01). **f**, MHC-I surface levels on IC-PE⁺ FDCs (central FDCs) or IC-PE⁻ (peripheral FDCs) 7 days after immunization (*n* = 9 mice; two experiments). Two-tailed paired *t*-test.

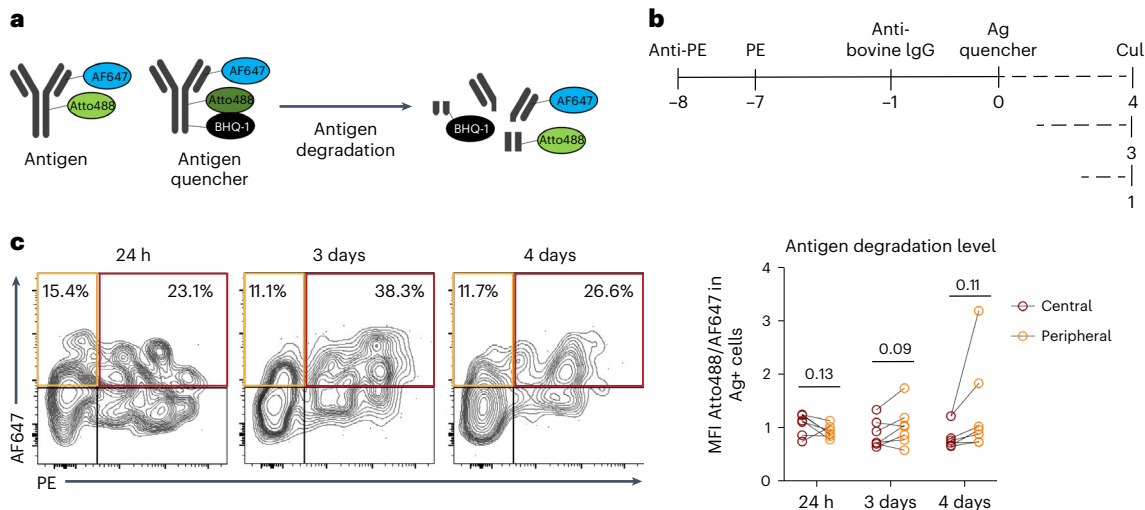


Fig. 5 | Central and peripheral LZ FDCs show a similarly low ability to degrade antigens. **a**, Schematics of the antigen-degradation sensor and a control sensor lacking the quencher. The antigen (bovine IgG) is covalently bound to AF647 and Atto488 dyes. The coupled BHQ-1 quencher absorbs Atto488 emission. Upon degradation, BHQ-1 is separated from Atto488, releasing its fluorescence from quenching. **b**, Immunization workflow to test the level of antigen degradation by central and peripheral LZ FDCs 24 h, 3 days and 4 days after immunization

with the IC-antigen-degradation sensor. **c**, Left: flow cytometry gating on central (red) and peripheral (orange) FDC populations. Right: levels of antigen-sensor degradation on central (IC-PE⁺ IC-antigen sensor⁺) FDCs; in red) and peripheral (IC-PE⁺ IC-antigen-sensor⁺) FDCs; in orange) FDCs in mice immunized as described in **b** (*n* = 7 mice, two experiments). Quantitative data show means \pm s.d. and analysis by two-tailed paired *t*-test.

marrow transplantation restricts the *Cr2*-deficiency to the FDC compartment^{36,37}. To analyze antigen binding to *Cr2*-deficient FDCs, we identified FDCs based on the expression of FCGR2B and VCAM1 (Extended Data Fig. 6c). FDCs from *Cr2*-KO mice did not express CR2 (Extended Data Fig. 6d) and showed negligible IC binding at 24 h or 7 days postimmunization (Extended Data Fig. 6e,f). Thus, the antigen-IC retention observed in this immunization model was exclusively CR2 dependent.

To understand if the ~ 1.5 -fold difference in CR2 levels on the cell surfaces of peripheral versus central FDCs (Fig. 3d and Extended Data Fig. 3a) could be responsible for different rates of antigen loss from these cells over time, we generated a stochastic model to predict the probability of IC survival on FDC surface over time as a function of CR2 surface density. The model used values from quantitative flow cytometry of CR2 (Extended Data Fig. 6g), CR2 dissociation (K_{OFF}) and association (K_{ON}) rates with C3dg—a C3 fragment closely resembling C3d—along with an estimated number of available C3d binding sites per IC (N_i) (Extended Data Fig. 6h). The model predicted that elevated CR2 levels proportionally increase the initial loading of ICs onto FDCs (Fig. 6b, left) and nonlinearly increase IC retention over the next 14 days. Plotting the inferred IC half-lives confirmed their sensitivity to CR2 density with a nonlinear rise starting around their physiological levels on FDCs (Fig. 6b, right). A 1.5-fold increase in CR2 density, from 250 to 375 molecules μm^{-2} , similar to the difference between peripheral and central FDCs, led to an increase in the apparent half-life of the IC on the FDC surface from 1.2 h to 1.5 days and in 6.7-fold higher levels of IC on day 14. Thus, even subtle differences in CR2 surface levels on FDCs can dramatically impact IC dissociation at long time scales.

To quantify the rates of IC loss from FDCs experimentally, we measured IC-488 antigen levels on peripheral and central FDCs from mice immunized first with IC-PE, then with IC-488 7 days later, and sacrificed 1, 4 or 7 days afterwards (Fig. 6c). Peripheral FDCs had less antigen on day 1 and the antigen disappeared faster thereafter as compared with the central FDCs, as the model had predicted.

We used two strategies to test the role of CR2 density in antigen retention. First, we used an anti-CD21/35 blocking antibody titrated to reduce the IC binding capacity on central LZ FDCs approximately by 50%, similar to the levels observed on the peripheral LZ FDCs in untreated mice (Extended Data Fig. 6i). Mice treated with blocking anti-CD21/35 antibodies were immunized with IC-PE and analyzed after 1, 4 or 7 days (Extended Data Fig. 6j). The treatment did not affect the numbers of the FDCs (Extended Data Fig. 6k and Fig. 6f); however, the percentage of FDCs loaded with IC-PE, and the antigen quantity decayed faster in the anti-CD21/35 treated mice (Fig. 6d–f), following kinetics similar to those of the peripheral FDCs in untreated mice (Fig. 6c). This effect was unlikely to be a consequence of disturbed GCs because blocking the GC does not affect antigen retention (Fig. 2d–f). Second, we manipulated CR2 levels selectively on FDCs by reconstituting lethally irradiated CD45.2 WT or *Cr2*-heterozygous (HET) mice with WT CD45.1/2 bone marrow and immunizing them with two subsequent antigen-ICs as above (Fig. 6g). Radioresistant FDCs from *Cr2*-HET mice expressed around 60% of WT CR2 levels (Fig. 6h). We observed a significant reduction in IC-PE quantity displayed by *Cr2*-HET FDCs 7 days after immunization, which was not observed at early time-points (IC-488) (Fig. 6i–k). Thus, *Cr2*-HET FDCs had a similar ability to

capture but an increased loss of ICs within 7 days after immunization compared with WT. To exclude that the reduction in CR2 expression could be affecting the development and maturation of FDCs, we analyzed FDCs from WT, *Cr2*-HET and *Cr2*-KO mice reconstituted with WT bone marrow cells. We observed normal FDC numbers, FCGR2B and VCAM1 expression, and network architecture between the three genotypes (Extended Data Fig. 6l,m).

Collectively, these data indicate that the small differences in the steady-state levels of CR2 expressed by peripheral and central FDCs result in preferential retention of antigens in the center of the follicle over time because of slower dissociation of ICs from central FDCs.

Repeated immunizations compete for CR2 on central FDCs

To determine how manipulation of FDC CR2 levels affects B cell responses to antigens, we bone-marrow reconstituted WT, *Cr2*-HET, and *Cr2*-KO mice with CD45.1 WT bone marrow cells, immunized them with NP-PE antigen-ICs and analyzed the GC response at day 20 postimmunization. We focused the analysis on CD45.1⁺ donor WT B cells, which were reconstituted similarly in all groups of mice. In mice where FDCs do not display the antigen (*Cr2*-KO), we observed a strong reduction in the percentage of GC B cells, class-switched IgG1⁺ GC B cells and NP-specific B cells compared with WT (Fig. 7a and Extended Data Fig. 7a,b,e). The intensity of B cell binding to NP as a readout of BCR affinity was also reduced in *Cr2*-KO mice (Fig. 7b) and so was the percentage of plasmablasts (PB) (Fig. 7c and Extended Data Fig. 7c). In contrast, the percentage of antigen-specific memory B cells was unaffected in *Cr2*-KO mice (Fig. 7d and Extended Data Fig. 7d), inducing a skewed differentiation output compared with WT mice (Fig. 7e). Consistently, the percentage of antigen-specific PCs in the bone marrow of the *Cr2*-KO mice was also reduced, even though the differences did not reach significance (Fig. 7f).

In the *Cr2*-HET animals, where antigens are lost faster from FDCs, there was a milder but consistent trend for reduction of the B cell response (Fig. 7a–f). In particular, the class-switched GC response was decreased significantly compared with WT mice, supporting the idea that antigen persistence promotes a prolonged GC response. Although we could not detect differences in BCR affinity in the *Cr2*-HET mice (Fig. 7b), there was a trend of reduced antigen-specific PB and PC differentiation contrasting with intact memory B cell differentiation (Fig. 7e,f), but this did not reach statistical significance. Thus, antigen display by FDCs is essential for generating a prolonged high-affinity antigen-specific GC response that supports PC differentiation. The duration of the antigen display is also important, although less than the initial FDC antigen capture, possibly because small amounts of retained antigen are sufficient to support the B cell response.

Since central FDCs are the exclusive site of long-term antigen retention that supports the GC response, we wondered whether they become saturated after repeated immunizations. We immunized mice consecutively with three (IC3; Fig. 7g) or four (IC4; Fig. 7h) differently labeled antigen-ICs at 1-week intervals and analyzed their FDCs 24 h

after the last immunization (Extended Data Fig. 7f). FDCs that retained all antigens showed the highest CR2 expression (Fig. 7g,h, left panels), suggesting that they correspond to the central FDCs. Indeed, imaging confirmed that all antigens older than a week were localized in the center of the follicle (Fig. 7j). In the three-dose regime, the central FDCs containing all antigens (IC-647, IC-488 and IC-PE) were found to be loaded with more of the last antigen (IC-PE) than FDCs containing only the last two (IC-488 and IC-PE, respectively), or only the last one (IC-PE) (Fig. 7g, right panel). This result matched our previous finding that central FDCs contain more antigen than peripheral FDCs 1 day after immunization (Fig. 6c). A similar phenomenon was detected in the four-dose regime, but only up to the third antigen, where the FDCs loaded with all antigens retained more IC-488 (the third antigen injected) than the other FDC populations (Fig. 7h, middle panel). However, these central FDCs could not efficiently capture the fourth antigen (IC-PE), displaying similar amounts of IC-PE as the peripheral FDCs that contained only this last antigen (Fig. 7h, right panel). Even though endogenous antibody responses against the injected xeno-antibodies could have cross-reactivity and possibly enhance IC formation in the subsequent doses, the selectivity of the saturation to the central FDCs suggests that this does not confound the interpretation. To quantify the saturation of central FDCs directly, we calculated the ratio of the amount of antigen on central versus peripheral FDCs from immunizations with 2, 3 or 4 ICs (Fig. 7i). This comparison confirmed that, after four doses, the capacity of antigen capture by central FDCs decreased to about half compared with the peripheral FDCs.

To understand whether old antigens also get displaced by new immunizations, we immunized mice with either one (1 IC) or four (4 IC) consecutive antigen-ICs (Extended Data Fig. 7g) and analyzed the presence of the first antigen on FDCs at the end of the experiment. The percentage of FDCs loaded with the first antigen-IC (IC-405) and the amount of IC-405 on these FDCs was lower when the mice were immunized with the three additional doses than when they were not. This suggests that the new antigens enhanced the dissociation of the first antigen from FDCs, although they did not replace it completely.

To understand whether the partial saturation and partial replacement of antigens on central FDCs modifies the B cell response to new antigens, we immunized mice with three subsequent antigen-ICs or only one antigen-IC and challenged them with IC-NP 21 days after the first immunization (Extended Data Fig. 7h). We tracked the antibody response to NP in the two groups of mice over the next 56 days. We observed that the high-affinity NP-specific IgG1 class-switched responses (Extended Data Fig. 7i) were similar between both groups of mice and so was the affinity maturation (Extended Data Fig. 7j). Thus, the partial saturation of the FDCs by the previous antigens does not impede the development of the B cell response to a new unrelated antigen.

Discussion

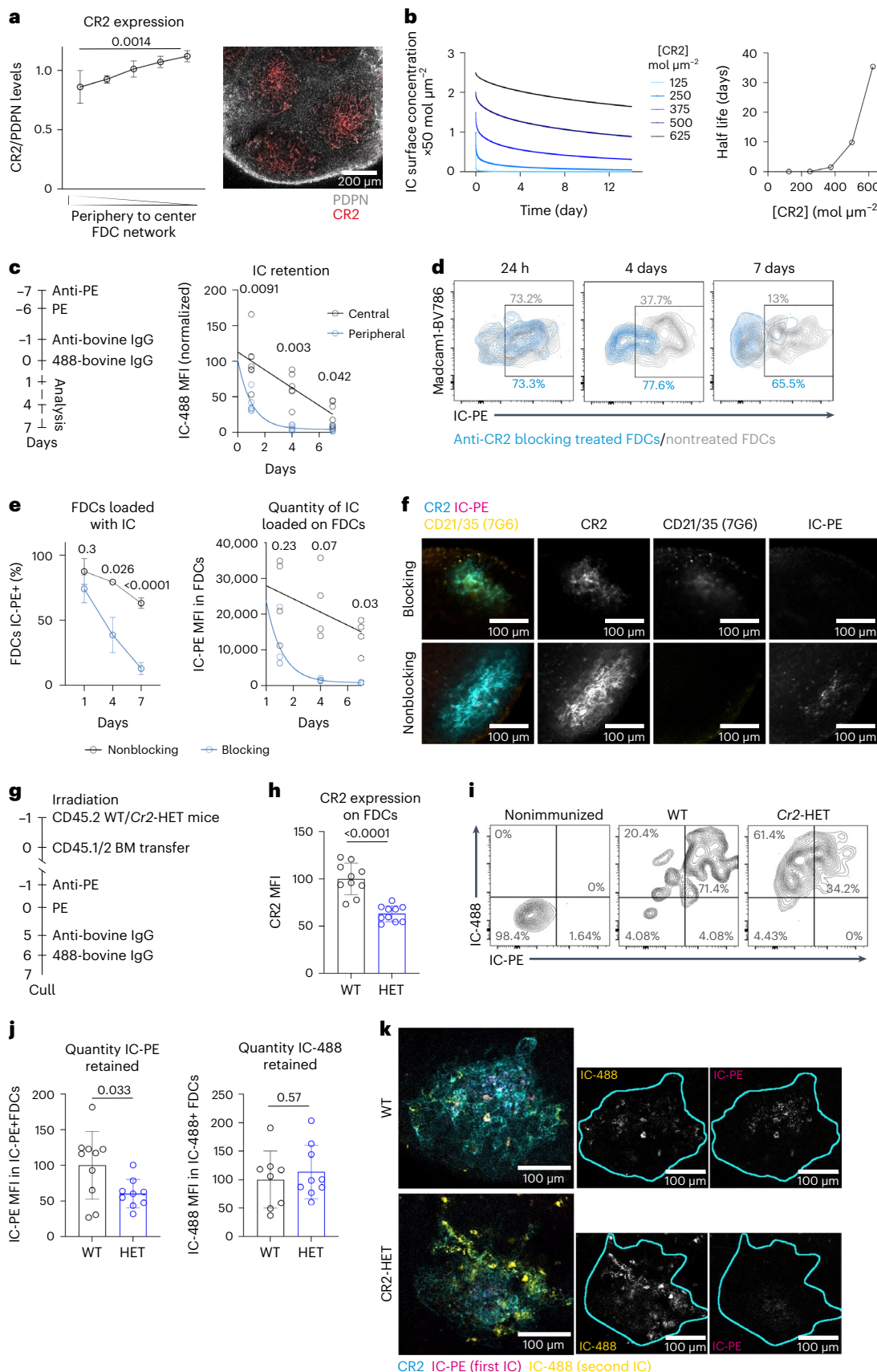
We demonstrate a topological heterogeneity in the FDC network that controls antigen retention in mouse LNs via levels of CR2. Peripheral

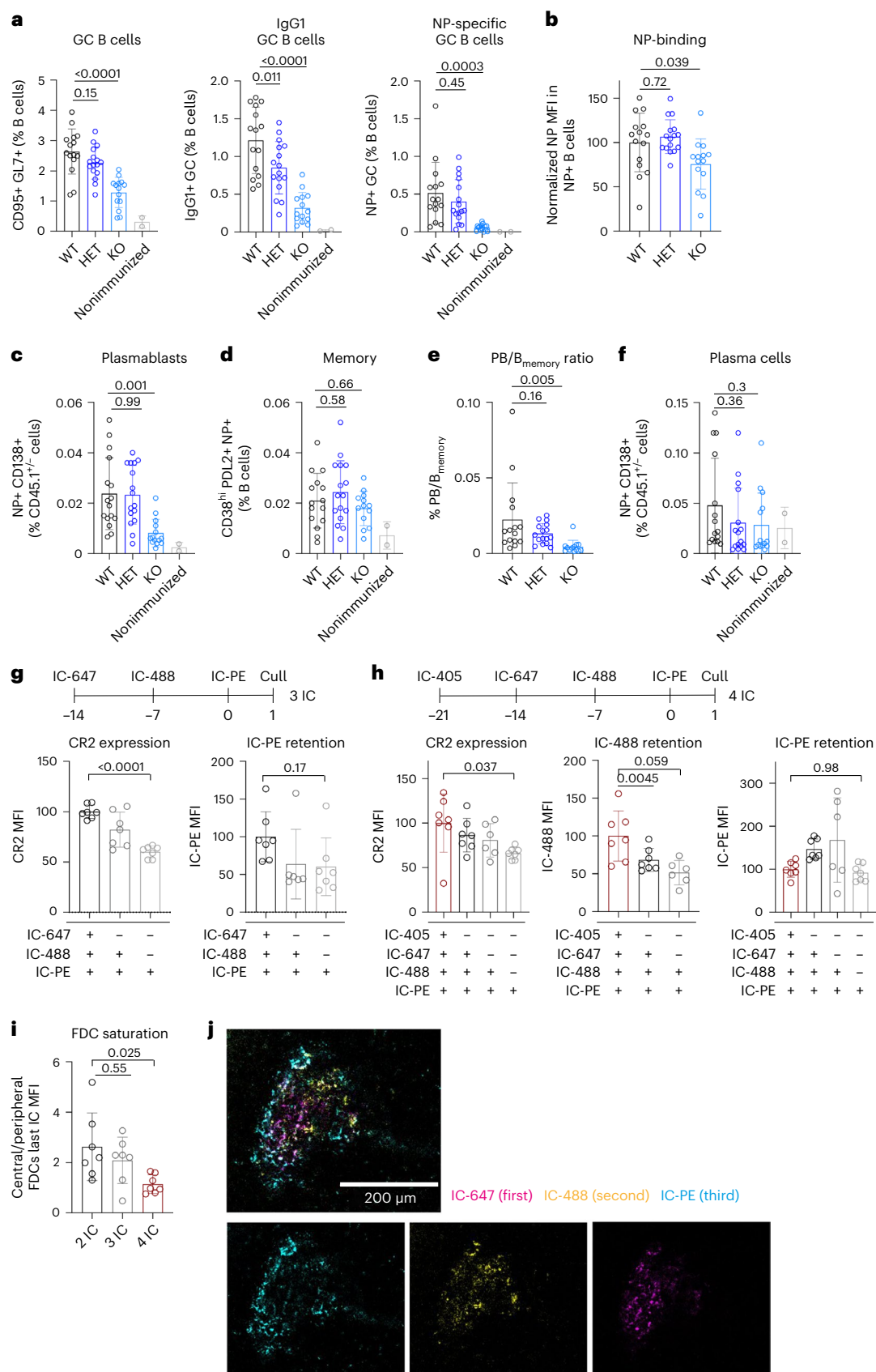
Fig. 6 | Membrane levels of CR2 dictate the half-life of antigen retention on peripheral and central FDCs. **a**, Quantification of CR2 levels on the FDC network in nonimmunized mice ($n = 4$ mice). The confocal image shows PDNP (gray) and CR2 (red). **b**, Modeling IC dissociation from FDC surfaces. Left: surface concentrations of ICs retained on FDCs over time depending on CR2 levels. Right: IC half-life versus CR2 surface concentration (molecules μm^{-2}). **c**, Rates of IC loss from central and peripheral LZ FDCs. Left: immunization workflow. Graphs show the quantity of the second IC retained by central FDCs (IC-PE⁺ IC-488⁺, in gray) and peripheral FDCs (IC-PE⁺ IC-488⁺, in blue) ($n = 7$ mice; two experiments). Lines show nonlinear regression fits to the data. **d**, Flow cytometry plots show IC-PE levels on gated FDCs from mice immunized with IC-PE and treated or not with anti-CD21/35 blocking antibody. **e**, Quantification of the percentage of IC-PE⁺ FDCs and quantity of IC-PE on the total FDCs ($n = 4$ mice) from mice treated as in **d**. **f**, Representative images ($n = 4$ mice) of FDC networks from LNs of mice treated

as in **d**. Anti-CD21/35 staining (7E9, cyan), IC-PE (magenta), injected anti-CD21/35 (7G7) antibody (yellow). Single-color images are shown in gray. **g**, Experimental workflow for measuring antigen retention by *Cr2*^{+/+} (WT) and *Cr2*^{-/-} (HET) FDCs. Bone-marrow reconstituted lethally irradiated CD45.2 WT and *Cr2*-HET mice were immunized with IC-PE and 7 days later with IC-488. **h**, CR2 membrane expression on FDCs from WT (black) and *Cr2*-HET (blue) mice as described in **g** ($n = 10$ mice). **i**, Gating strategy to analyze the IC loading in nonimmunized WT mice, and WT or *Cr2*-HET mice immunized as in **g**. **j**, Quantity of IC loaded on total FDCs from WT ($n = 10$) and *Cr2*-HET ($n = 9$) mice following the experimental workflow described in **g**. **k**, Representative images of FDC networks from mice treated as described in **g**. CR2 (cyan), IC-PE (magenta), IC-488 (yellow). Single-color images are shown in gray. Cyan line demarcates the FDC network boundary. All quantitative data show means \pm s.d. and analysis by two-tailed unpaired *t*-test and two-way ANOVA.

CR2-low FDCs retain antigens for the first few days postimmunization, while central CR2-high FDCs preserve antigens for weeks, creating a reservoir of previous immunizations in the GC. A similar pattern of antigen localization can be observed in the mouse spleen³⁸ and in primate

LNs³⁹, suggesting that topological heterogeneity of FDCs is a common feature of B cell follicles. Although our data did not distinguish whether central and peripheral FDCs represent distinct developmental subsets or a spatial gradient within a single population, the results indicate that





spatial organization of the stroma contributes to the orchestration of B cell responses.

We show that the spatial FDC heterogeneity lies within the LZ FDC subset. Central FDCs likely relate to activated FDCs observed in the GC

LZ of secondary follicles²². Formation of the GC may be one mechanism to establish this FDC spatial patterning, for example, by enhanced production of LT α 1 β 2 by GC B cells⁴⁰. However, acute blockade of the GC and FDC activation using anti-CD40L antibodies did not affect

Fig. 7 | Antigen display by FDCs regulates the B cell response while successive immunizations partially saturate central FDCs. **a**, Percentages of GC B cells (CD95⁺ GL7⁺), IgG1⁺ GC B cells and NP-specific GC B cells in the LNs of WT (black; $n = 15$ mice), *Cr2*-HET (dark blue; $n = 16$ mice) and *Cr2*-KO (light blue; $n = 14$ mice) mice reconstituted with WT CD45.1⁺ donor bone marrow and immunized with IC NP-PE 20 days before analysis. Cells were gated on CD45.1⁺ B220⁺ donor cells. **b**, Quantification of the NP-PE MFI in NP⁺ B cells from mice described in **a**. **c**, Percentage of plasmablasts (CD138⁺ NP⁺ within CD45.1^{+/−}) from mice described in **a**. **d**, Percentage of memory B cells from mice described in **a**. **e**, Quantification of plasmablast to memory B cells ratio in WT (black), *Cr2*-HET (dark blue) and *Cr2*-KO (blue light) mice treated as described in **a**. **f**, Quantification of bone marrow PCs (NP⁺ CD138⁺ in B220[−] TCR β [−]) from mice described in **a**. **g**, Schematic workflow of mice consecutively immunized with three distinct ICs. Plots show

CR2 expression and retention of the last injected IC (IC-PE) in the different FDC subsets identified by the presence of all the three injected ICs (black), the last two ICs (dark gray) or only the last one (light gray) ($n = 7$ mice). **h**, Schematic workflow of mice injected consecutively with four different ICs. Plots show CR2 expression and retention of the penultimate IC (IC-488) or the last IC (IC-PE) in the FDC subsets containing four injected ICs (red), the last three ICs (black), the last two ICs (dark gray) or only the last IC (light gray); ($n = 7$ mice). **i**, Quantification of the central FDC saturation by measuring the ratio between the quantities of the last IC on central and peripheral FDCs in mice immunized with two, three or four ICs; ($n = 7$ mice). **j**, Confocal image of an FDC network from a mouse immunized with three different fluorescent antigen-ICs as described in **g**. All quantitative data show means \pm s.d. and analysis by two-tailed one-way ANOVA with multiple comparisons.

CR2 levels or antigen retention. Alternatively, FDC patterning can be induced by FDC network remodeling. We show that, in agreement with previous data¹⁰, immunization expands the FDC network. New FDCs arise from precursors near the subcapsular sinus^{10,41}, potentially creating a centripetal maturation pattern. However, we could distinguish peripheral and central FDCs even before immunization, suggesting constitutive patterning, possibly induced by steady-state reactivity against endogenous antigens^{42,43}. This notion is supported by the disruption of FDC organization in BCR Tg mice, which are unable to respond to most antigens. Studies using new genetic tools to map the origin and development of peripheral and central FDCs will be required to dissect these mechanisms in the future.

We corroborated the functional heterogeneity within LZ FDCs by single-cell transcriptomics. A cellular cluster resembling peripheral FDCs expressed genes regulating cytokine responses, indicating they are responsive to immune stimuli. In contrast, a cluster enriched in markers of central FDCs showed expression of genes regulating oxidative phosphorylation and the cytoskeleton. The latter could result in higher membrane stiffness, which enhances B cell affinity discrimination⁴⁴. The central FDC cluster also expressed genes involved in the processing and presentation of antigens on MHC I and II, mirroring findings in human FDCs⁴⁵. This suggests that central FDCs may interact with CD8 and CD4 T cells, although the relevance of this needs to be further investigated.

We show that the main factor that drives the selective retention of antigens by central FDCs is the higher expression of CR2 on their surfaces. The interactions of CR2 with C3d are transient ($K_D \sim 140$ nM, half-life ~6 s), mandating that long-term IC retention involves multivalent binding. Modeling indicates that the IC dissociation half-life rises sharply when CR2 exceeds ~250 molecules μm^{-2} , typical of the levels detected on FDCs. A difference in avidity may also underlie FDC acquisition of ICs from noncognate B cells¹⁹, which express only ~20 CR2 molecules μm^{-2} . It is likely that CR2 avidity works in conjunction with the recycling of ICs into nondegradative endosomes^{46,47} and with the exclusion of extracellular proteases from the B cell follicle⁴⁸. However, antigen degradation was similarly low between peripheral and central FDCs, suggesting that these factors do not contribute to spatial patterning. Similarly, enhanced FCGR2B expression by central FDCs did not seem to contribute to IC retention, which was exclusively CR2 dependent, consistently with previous data⁴⁹. However, FCGR2B may play a regulatory role in the B cell response or become important upon reimmunization or in autoimmunity^{25,50,51}.

Although GC reactions can develop independently of antigen binding to FDCs^{29,52}, we show that FDC antigen retention promoted long-lasting GC responses with higher PB output and BCR affinity. This agrees with the reported importance of FDC-expressed CR2 for vaccines-induced antibody responses²⁷ and with enhanced GC responses induced by vaccines designed to increase antigen deposition on FDCs^{30–32}. In contrast, memory B cells were unaffected by the absence of FDC antigen retention. Since limiting access of activated B cells to antigen promotes their differentiation into memory B cells^{53,54},

rapid antigen loss from FDCs may also favor the differentiation of memory B cells. Therefore, vaccine designs enhancing antigen persistence on FDCs could also skew the memory/PB ratio.

We show that repeated IC injections partially saturated central FDCs, although a small amount of new antigens could still be deposited by replacing old antigens. In contrast, peripheral FDCs remained fully receptive to new antigens and may assist the B cell response when central FDCs become saturated. Total FDC antigen capture indeed was more important for the GC than prolonged retention, based on the GC phenotypes of FDC *Cr2*-KO versus *Cr2*-HET mice. We propose that the FDC network handles repeated challenges using a range of CR2 levels, keeping a dynamic repository of past antigens but also remaining receptive to new ones, which contrasts with the idea of saturable FDC niches for GC development⁵⁵.

Illuminating the mechanisms that regulate the development of central and peripheral FDCs, their CR2 levels and other functions will advance the understanding of the role of the follicular stroma in B cell responses to immunizations, infections and cancers. Engineering vaccines for high CR2 avidity may enhance FDC retention and immune protection^{56,57}. Blocking CR2 binding, in contrast, may effectively displace old antigens from FDCs and terminate unwanted responses, such as in autoimmune diseases.

Online content

Any methods, additional references, Nature Portfolio reporting summaries, source data, extended data, supplementary information, acknowledgements, peer review information; details of author contributions and competing interests; and statements of data and code availability are available at <https://doi.org/10.1038/s41590-023-01559-1>.

References

1. Victora, G. D. & Nussenzweig, M. C. Germinal centers. *Annu Rev Immunol.* **40**, 413–442 (2022).
2. Gitlin, A. D., Shulman, Z. & Nussenzweig, M. C. Clonal selection in the germinal centre by regulated proliferation and hypermutation. *Nature* **509**, 637–640 (2014).
3. Victora, G. D. et al. Germinal center dynamics revealed by multiphoton microscopy with a photoactivatable fluorescent reporter. *Cell* **143**, 592–605 (2010).
4. Batista, F. D. & Harwood, N. E. The who, how and where of antigen presentation to B cells. *Nat. Rev. Immunol.* **9**, 15–27 (2009).
5. Mueller, S. N. & Germain, R. N. Stromal cell contributions to the homeostasis and functionality of the immune system. *Nat. Rev. Immunol.* **9**, 618–629 (2009).
6. Pikor, N. B. et al. Remodeling of light and dark zone follicular dendritic cells governs germinal center responses. *Nat. Immunol.* **21**, 649–659 (2020).
7. Rodda, L. B. et al. Single-cell RNA sequencing of lymph node stromal cells reveals niche-associated heterogeneity. *Immunity* **48**, 1014–1028.e6 (2018).

8. Alexandre, Y. O. et al. A diverse fibroblastic stromal cell landscape in the spleen directs tissue homeostasis and immunity. *Sci. Immunol.* **7**, eabj0641 (2022).
9. Krautler, N. J. et al. Follicular dendritic cells emerge from ubiquitous perivascular precursors. *Cell* **150**, 194–206 (2012).
10. Jarjour, M. et al. Fate mapping reveals origin and dynamics of lymph node follicular dendritic cells. *J. Exp. Med.* **211**, 1109–1122 (2014).
11. Pasparakis, M., Alexopoulou, L., Episkopou, V. & Kollias, G. Immune and inflammatory responses in TNF alpha-deficient mice: a critical requirement for TNF alpha in the formation of primary B cell follicles, follicular dendritic cell networks and germinal centers, and in the maturation of the humoral immune response. *J. Exp. Med.* **184**, 1397–1411 (1996).
12. Hir, M. L. et al. Differentiation of follicular dendritic cells and full antibody responses require tumor necrosis factor receptor-1 signaling. *J. Exp. Med.* **183**, 2367–2372 (1996).
13. Wang, Y., Wang, J., Sun, Y., Wu, Q. & Fu, Y.-X. Complementary effects of TNF and lymphotoxin on the formation of germinal center and follicular dendritic cells. *J. Immunol.* **166**, 330–337 (2001).
14. Tumanov, A. V., Kuprash, D. V., Mach, J. A., Nedospasov, S. A. & Chervonsky, A. V. Lymphotoxin and TNF produced by B Cells are dispensable for maintenance of the follicle-associated epithelium but are required for development of lymphoid follicles in the Peyer's patches. *J. Immunol.* **173**, 86–91 (2004).
15. Wang, X. et al. Follicular dendritic cells help establish follicle identity and promote B cell retention in germinal centers. *J. Exp. Med.* **208**, 2497–2510 (2011).
16. Lu, E., Wolfreys, F. D., Muppudi, J. R., Xu, Y. & Cyster, J. G. S-Geranylgeranyl-l-glutathione is a ligand for human B cell-confinement receptor P2RY8. *Nature* **567**, 244–248 (2019).
17. Suzuki, K. et al. The sensing of environmental stimuli by follicular dendritic cells promotes immunoglobulin a generation in the gut. *Immunity* **33**, 71–83 (2010).
18. Kranich, J. et al. Follicular dendritic cells control engulfment of apoptotic bodies by secreting Mfge8. *J. Exp. Med.* **205**, 1293–1302 (2008).
19. Phan, T. G., Grigorova, I., Okada, T. & Cyster, J. G. Subcapsular encounter and complement-dependent transport of immune complexes by lymph node B cells. *Nat. Immunol.* **8**, 992–1000 (2007).
20. Ferguson, A. R., Youd, M. E. & Corley, R. B. Marginal zone B cells transport and deposit IgM-containing immune complexes onto follicular dendritic cells. *Int. Immunol.* **16**, 1411–1422 (2004).
21. Rodda, L. B., Bannard, O., Ludewig, B., Nagasawa, T. & Cyster, J. G. Phenotypic and morphological properties of germinal center dark zone Cxcl12-expressing reticular cells. *J. Immunol.* **195**, 4781–4791 (2015).
22. Allen, C. D. C. & Cyster, J. G. Follicular dendritic cell networks of primary follicles and germinal centers: phenotype and function. *Semin. Immunol.* **20**, 14–25 (2008).
23. Shikh, M. E. E., Sayed, R. E., Szakal, A. K. & Tew, J. G. Follicular dendritic cell (FDC)-FcγRIIB engagement via immune complexes induces the activated FDC phenotype associated with secondary follicle development. *Eur. J. Immunol.* **36**, 2715–2724 (2006).
24. Tokatlian, T. et al. Innate immune recognition of glycans targets HIV nanoparticle immunogens to germinal centers. *Science* **363**, 649–654 (2019).
25. van der Poel, C. E. et al. Follicular dendritic cells modulate germinal center B cell diversity through FcγRIIB. *Cell Rep.* **29**, 2745–2755.e4 (2019).
26. Gonzalez, S. F. et al. Complement-dependent transport of antigen into B cell follicles. *J. Immunol.* **185**, 2659–2664 (2010).
27. Fang, Y., Xu, C., Fu, Y. X., Holers, V. M. & Molina, H. Expression of complement receptors 1 and 2 on follicular dendritic cells is necessary for the generation of a strong antigen-specific IgG response. *J. Immunol.* **160**, 5273–5279 (1998).
28. Brockman, M. A., Verschoor, A., Zhu, J., Carroll, M. C. & Knipe, D.M. Optimal long-term humoral responses to replication-defective herpes simplex virus require CD21/35 complement receptor expression on stromal cells. *J. Virol.* **80**, 7111–7117 (2006).
29. Hannum, L. G., Haberman, A. M., Anderson, S. M. & Shlomchik, M. J. Germinal center initiation, variable gene region hypermutation, and mutant B cell selection without detectable immune complexes on follicular dendritic cells. *J. Exp. Med.* **192**, 931–942 (2000).
30. Kato, Y. et al. Multifaceted effects of antigen valency on B cell response composition and differentiation in vivo. *Immunity* **53**, 548–563.e8 (2020).
31. Martin, J. T. et al. Targeting HIV Env immunogens to B cell follicles in nonhuman primates through immune complex or protein nanoparticle formulations. *npj Vaccines* **5**, 72 (2020).
32. Lee, J. H. et al. Long-primed germinal centres with enduring affinity maturation and clonal migration. *Nature* **609**, 998–1004 (2022).
33. Foy, T. M. et al. gp39-CD40 interactions are essential for germinal center formation and the development of B cell memory. *J. Exp. Med.* **180**, 157–163 (1994).
34. Szklarczyk, D. et al. STRING v11: protein–protein association networks with increased coverage, supporting functional discovery in genome-wide experimental datasets. *Nucleic Acids Res.* **47**, D607–D613 (2019).
35. Martínez-Riaño, A. et al. Antigen phagocytosis by B cells is required for a potent humoral response. *EMBO Rep.* **19**, e46016 (2018).
36. Endres, R. et al. Mature follicular dendritic cell networks depend on expression of lymphotoxin β receptor by radioresistant stromal cells and of lymphotoxin β and tumor necrosis factor by B cells. *J. Exp. Med.* **189**, 159–168 (1999).
37. Kapasi, Z. F., Kosco-Vilbois, M. H., Shultz, L. D., Tew, J. G. & Szakal, A. K. Cellular origin of follicular dendritic cells. *Adv. Exp. Med. Biol.* **355**, 231–235 (1994).
38. Gordon, L. et al. Foot-and-mouth disease virus localisation on follicular dendritic cells and sustained induction of neutralising antibodies is dependent on binding to complement receptors (CR2/CR1). *PLoS Pathog.* **18**, e1009942 (2022).
39. Cirelli, K. M. et al. Slow delivery immunization enhances HIV neutralizing antibody and germinal center responses via modulation of immunodominance. *Cell* **177**, 1153–1171.e28 (2019).
40. Ansel, K. M. et al. A chemokine-driven positive feedback loop organizes lymphoid follicles. *Nature* **406**, 309–314 (2000).
41. Prados, A. et al. Fibroblastic reticular cell lineage convergence in Peyer's patches governs intestinal immunity. *Nat. Immunol.* **22**, 510–519 (2021).
42. Zikherman, J., Parameswaran, R. & Weiss, A. Endogenous antigen tunes the responsiveness of naïve B cells but not T cells. *Nature* **489**, 160–164 (2012).
43. Noviski, M. et al. Optimal development of mature B cells requires recognition of endogenous antigens. *J. Immunol.* **203**, 418–428 (2019).
44. Spillane, K. M. & Tolar, P. B cell antigen extraction is regulated by physical properties of antigen-presenting cells. *J. Cell Biol.* **216**, 217–230 (2017).
45. Heesters, B. A. et al. Characterization of human FDCs reveals regulation of T cells and antigen presentation to B cells. *J. Exp. Med.* **218**, e20210790 (2021).
46. Arulraj, T., Binder, S. C. & Meyer-Hermann, M. Rate of immune complex cycling in follicular dendritic cells determines the extent of protecting antigen integrity and availability to germinal center B cells. *J. Immunol.* **206**, ji2001355 (2021).

47. Heesters, B. A. et al. Endocytosis and recycling of immune complexes by follicular dendritic cells enhances B cell antigen binding and activation. *Immunity* **38**, 1164–1175 (2013).
48. Aung, A. et al. Low protease activity in B cell follicles promotes retention of intact antigens after immunization. *Science* **379**, eabn8934 (2023).
49. Suzuki, K., Grigorova, I., Phan, T. G., Kelly, L. M. & Cyster, J. G. Visualizing B cell capture of cognate antigen from follicular dendritic cells. *J. Exp. Med.* **206**, 1485–1493 (2009).
50. Barrington, R. A., Pozdnyakova, O., Zafari, M. R., Benjamin, C. D. & Carroll, M. C. B lymphocyte memory: role of stromal cell complement and Fc γ RIIB receptors. *J. Exp. Med.* **196**, 1189–1199 (2002).
51. Qin, D. et al. Fc γ receptor IIB on follicular dendritic cells regulates the B cell recall response. *J. Immunol.* **164**, 6268–6275 (2000).
52. Ahearn, J. M. et al. Disruption of the Cr2 locus results in a reduction in B-1a cells and in an impaired B cell response to T-dependent antigen. *Immunity* **4**, 251–262 (1996).
53. Viant, C. et al. Antibody affinity shapes the choice between memory and germinal center B cell fates. *Cell* **183**, 1298–1311.e11 (2020).
54. Glaros, V. et al. Limited access to antigen drives generation of early B cell memory while restraining the plasmablast response. *Immunity* **54**, 2005–2023.e10 (2021).
55. Avancena, P. et al. The magnitude of germinal center reactions is restricted by a fixed number of preexisting niches. *Proc. Natl Acad. Sci. USA* **118**, e2100576118 (2021).
56. Klein, F. et al. Somatic mutations of the immunoglobulin framework are generally required for broad and potent HIV-1 neutralization. *Cell* **153**, 126–138 (2013).
57. Pappas, L. et al. Rapid development of broadly influenza neutralizing antibodies through redundant mutations. *Nature* **516**, 418–422 (2014).

Publisher's note Springer Nature remains neutral with regard to jurisdictional claims in published maps and institutional affiliations.

Springer Nature or its licensor (e.g. a society or other partner) holds exclusive rights to this article under a publishing agreement with the author(s) or other rightsholder(s); author self-archiving of the accepted manuscript version of this article is solely governed by the terms of such publishing agreement and applicable law.

© The Author(s), under exclusive licence to Springer Nature America, Inc. 2023

Methods

Mice

C57BL/6, *Cr2*-KO (*Cr2*^{tm1Hmo}), CXCL13-TdTomato (Tg(*Cxcl13*-Cre/tdTomato)719Biat), B1-8fl (Igh^{tm4Cgn} Igk^{Ctm1Cgn/tm1Cgn}), MD4 (C57BL/6 Tg(*ghelMD4*4Ccg/J) and CD45.1 (B6.SJL-*Ptprc*^a *Pepc*^b /BoyJ) mice were used. To obtain *Cr2*-HET and CD45.1/CD45.2 mice, *Cr2*-KO and CD45.1 mice were bred with C57BL/6 mice. IgH^{B1-8fl} IgK^{-/-} (B1-8fl) mice have a rearranged VDJ gene segment inserted into the Ig heavy chain (IgH) locus and a neomycin resistance cassette replacing the exon encoding the constant region of the immunoglobulin kappa chain, which guarantees that most B cells express a BCR recognizing 4-hydroxy-3-nitrophenyl acetyl hapten (NP). IgHEL-MD4 (MD4) mice express HyHEL10 immunoglobulin heavy and light chains transgenes so that most B cells recognize hen egg-white lysozyme antigen (HEL). All experiments were approved by the Francis Crick Institute and UCL Ethical Review Panels and the UK Home Office using age- and sex-related mice.

To generate bone marrow chimaeras, recipient mice were lethally irradiated with two doses of 5 Gy and reconstituted with 5×10^6 donor bone marrow cells by intravenous injection. Reconstituted mice were fed with 0.2 mg ml⁻¹ Baytril (Enrofloxacin) in their drinking water for 4 weeks postreconstitution.

Immunization

Mice were immunized intraperitoneally (i.p.) with 2 mg anti-antigen antibody in 200 μ l of PBS (Rabbit anti-B-Phycoerythrin, catalog no. 100-4199, Rockland; donkey anti-goat IgG, catalog no. 705-001-003, Jackson ImmunoResearch; rabbit anti-human IgG, catalog no. 309-001-003, Jackson ImmunoResearch; anti-bovine IgG, catalog no. 301-001-003, Jackson ImmunoResearch). After 18 h, mice were injected subcutaneously with 10 μ g of fluorescent antigen (R-Phycoerythrin cat. P801, ThermoFisher; NP-Phycoerythrin catalog no. N-5070-1, LGC Biosearch Technologies; goat Fab2 IgG anti-horse, catalog no. 108-006-003, Jackson ImmunoResearch; rabbit anti-human IgG, catalog no. 309-001-003, Jackson ImmunoResearch; rabbit anti-bovine IgG, catalog no. 301-001-003, Jackson ImmunoResearch) in 100 μ l mixed 1:1 with Imject Alum Adjuvant (catalog no. 77161 ThermoFisher) in the upper and lower flank to target the brachial, axillary and inguinal draining LNs. Mouse tissues were analyzed by flow cytometry, confocal microscopy and enzyme-linked immunosorbent assay (ELISA) at different timepoints after immunization.

Cellular isolation

For FDCs preparation, draining LNs were disaggregated into small pieces with 25G needles and collected in RPMI-1640 medium containing 2% FCS, 20 mM HEPES pH 7.2, 0.1 mg ml⁻¹ collagenase P (Roche) and 25 μ g ml⁻¹ DNase I (Sigma). Dissociated tissue was incubated at 37 °C for 60 min, recollecting supernatant every 15 min. After enzymatic digestion, cell suspensions were filtered using a 100 μ m strainer and washed with PBS containing 0.5% FCS and 10 mM EDTA. Cell suspensions were used directly for staining with antibodies.

For B cell isolation, spleens were disaggregated using 40 μ m strainer and treated with ammonium-chloride-potassium lysis buffer (AcK; made in house) for 5 min. Single-cell suspension was subsequently incubated with CD43 microbeads (Miltenyi Biotech), following the manufacturer's instructions.

Staining

For flow cytometry staining, single-cell suspension was incubated with Fixable Viability Dye-e506 (Invitrogen) for 15 min in PBS. Cells were subsequently incubated with anti-CD16/32 (purified or labeled) and the appropriate antibodies for 20 min at 4 °C in PBS containing 0.5% FCS and 10 mM EDTA for FDC analysis or PBS containing 2% FCS and 2 mM EDTA for B cell analysis. The following antibodies were used for FDC and B cell phenotyping: B220 (clone RA3-6B2, Biolegend), CD45.2

(104, Biolegend), CD21/35 (7E9, Biolegend), PDPN (8.1.1, Biolegend), Madcam1 (MECA-367, BD Biosciences), CD31 (390, Biolegend), CD23 (B3B4, BD Biosciences), H2-Kb/Kd (28-8-6, Biolegend), CD95 (Jo2, BD Pharmigen), IgD (11-23c, Biolegend), T and B cell activation antigen (GL7, BD Biosciences), CD45.1 (A20, Biolegend), CD138 (281-2, Biolegend), CD38 (90, Biolegend), PDL-2 (TY25, BD Horizon), IgG1 (RMG1-1, Biolegend), IgM (R6-60.2, BD Biosciences). Cells were analyzed using an LSRIFortessa flow cytometer and analyzed using FlowJo. FDCs were gated by excluding hematopoietic cells (CD45⁺ PDPN⁻) and specifically B cells (B220⁺), and selecting those stromal cells (PDPN⁺), non-endothelial (CD31⁻), expressing high levels of CR2 (CD21/35hi) and Madcam1⁺ integrin receptor. Samples were acquired on an LSRIFortessa (BD Biosciences) using BD FACSDiva software v.8.0.1. For cell sorting experiments for scRNASeq, cells were sorted using FACS Aria Fusion and collected in PBS + 0.05% BSA. For analyzing CR2 surface expression on FDCs and B cells by quantitative flow cytometry, LN dissociated cells were incubated with a surface antibody mix (anti-B220, anti-CD45.2, anti-PDPN, anti-CD31, anti-Madcam1) containing anti-CD21/35-PE under saturation conditions. PE Phycoerythrin Fluorescence Quantitation Kit containing beads conjugated with four levels of PE was used to obtain a calibration curve from which the number of CR2 surface molecules in the cells of interest could be calculated. Surface CR2 density was calculated based on the calculated number of CR2 molecules per cell divided by the cell surface area measured using Imagestream.

For microscopy staining, LNs were incubated 4 h with Antigenfix solution (Diapath) and washed and permeabilized in PBS containing 1% BSA, 1% normal mouse sera and 2% Triton X-100 for 24 h. LNs were incubated with the antibody mix in the permeabilization buffer for 3 days at 22 °C while shaking. Organs were subsequently washed in permeabilization buffer for 24 h and incubated with RapiClear solution (1.47 RIN) for 24 h at RT. Clarified organs were imaged mounted in RapiClear solution using Leica SP5 Upright or Leica SP8 Falcon Inverted microscopes. For PDPN staining, LNs were permeabilized in 4% SDS in 200 mM boric acid at 37 °C for 4 h and labeled in 4% SDS solution for 4 days at 22 °C as previously described in ref. 58.

For microscopy of sections, LNs were embedded in OCT and frozen at -80 °C for at least 24 h. sections 20 μ m were obtained using the Cryotome (Leica) and fixed in 4% paraformaldehyde for 15 min. Sections were blocked using 2% BSA + 5% FBS in PBS (blocking buffer) for 1 h at 22 °C and incubated for 2 h with the following antibodies: anti-PD1 (29.F.1A12) and anti-CD21/35 (7E9) from Biolegend, and GL7 and anti-Bcl6 (K112-91) from BD Biosciences. The FDCM1 staining was performed in three subsequent steps: tissues were first stained with anti-FDCM1 (BD) in blocking buffer, and after washing, sections were incubated with anti-rat-AF488 (Cell Signaling; 1/400) for 1 h in blocking buffer, and finally were incubated with anti-CD21/35 antibody (Biolegend).

Droplet-based single-cell RNA sequencing analysis

Sorted CXCL13-TdTomato⁺ PDPN⁺ live cells were run using the 10x Chromium (10x Genomics) system, and cDNA libraries were generated according to the manufacturer's recommendations (Chromium Single-Cell 3' Reagent Kit (v.3.1 Chemistry)). Libraries were sequenced via Hiseq 4000 for Illumina sequencing. Raw sequencing data were processed using the CellRanger pipeline v.3 (10x Genomics) with the Ensembl GRCm38 release 89 reference transcriptome. Count tables were loaded into R and further processed using the Seurat R package v.3.1.5 (ref. 59). Samples were pooled from three independent experiments (Cxcl13-Td immunized for 24 h, LNs from six mice pooled; Cxcl13-Td immunized for 7 days with a first antigen-ICs and 24 h with a second antigen-ICs, LNs from six mice pooled). Subsequently, cells containing fewer than 200 distinct genes and cells with more than 10% of unique molecular identifiers stemming from mitochondrial genes were excluded. Furthermore, cells that featured at least one read count for *Lyve1*, *Hba-a1*, *Hba-a2*, *Krt18*, *Trac*, *Cd3d*, *Cldn5*, *Ly6c1*,

Egfl7, *Ptprc*, *S100b*, *Cd79a* and *Cd79b* genes were removed to eliminate contaminating hematopoietic cells, erythrocytes, and endothelial and epithelial cells as previously described⁶. After quality control and removal of contaminants, the remaining cells were retained for further processing using the default method from the Seurat package (v.3.1.5). Clusters were characterized based on described markers^{6,7}. Differentially expressed genes between three FDC clusters were performed using Seurat within the samples from Cxcl13-Td mice immunized for 7 days. Pathways enriched among their differentially expressed genes (greater than twofold increased expression; adjusted $P < 0.05$) were analyzed using STRING³⁴.

Image analysis

To study antigen distribution within the FDC network, acquired datasets were analyzed using MATLAB with ImageJ plugin. Images were subsampled in the x and y axis ($4\times$) and a filtered to generate a mask of the FDC networks based on CD21 staining. Individual follicles were detected, labeled, and segmented into six concentric shells with the most peripheral serving as background. Antigen fluorescence was measured in the five inner rings, background subtracted, mean-normalized and then normalized by the anti-CD21 staining processed in the same manner.

To analyze FDC network volume, images from clarified organs were analyzed using Imaris where FDC networks were detected based on thresholded CD21 staining.

Protein labeling with dyes

Antibodies were conjugated to one of several fluorophores (AlexaFluor 405, AlexaFluor 488, AlexaFluor 647 NHS esters (ThermoFisher)) in sodium carbonate buffer, according to the manufacturer's instructions. Excess dye was removed using Zeba 7K MWCO desalting columns (Pierce, ThermoFisher).

For the degradation sensor, antigen was conjugated first with AlexaFluor 647 and AlexaFluor 488 NHS esters (ThermoFisher) and with BHQ-1 quencher as previously described⁵⁰.

In vitro antigen degradation assay

Conjugated bovine IgG with AlexaFluor 647 and AlexaFluor 488 NHS esters (control) and bovine IgG conjugated with AlexaFluor 647 and AlexaFluor 488 NHS esters and BHQ-1 NHS ester (ratio 1 IgG: 9 BHQ-1 molecules) were treated at 50 °C for 30 min and 95 °C for 5 min with 2 mg ml⁻¹ Proteinase K. Fluorescent emission was measured using the Spark multimode plate reader (Tecan).

Ex vivo degradation assay

Carboxylated latex beads (50×10^6 ; 1 μm in diameter) were incubated overnight with a concentration of 20 $\mu\text{g ml}^{-1}$ of anti-IgM plus 20 $\mu\text{g ml}^{-1}$ antigen-quencher or only anti-IgM in 1 ml of PBS at 4 °C.

Naïve purified B cells were resuspended in complete RPMI buffer (10% FBS, 100 μM nonessential amino acids (ThermoFisher), 2 mM L-Glutamine (ThermoFisher), 50 μM 2-mercaptoethanol (ThermoFisher) and penicillin-streptomycin (GE Healthcare Life Sciences)) and plated in 96-well V-bottom plates at a concentration of 0.5×10^6 cells in 50 μl . Antibody-coated beads were added to reach a bead:cell ratio of 3:1. The cellular and bead suspension were briefly centrifuged at 400g and were incubated at 37 °C for different timepoints. Subsequently, cells were washed and stained on ice³⁵.

HIV-multimeric nanoparticles

SpyCatcher SpyTag 60-mer particles were generated as described⁶¹. Briefly, monomeric SpyCatcher-mi3 (kindly donated by M. Howarth) was incubated with a three times molar excess of YU-gp120-SpyTag HIV envelope protein for 18 h at 25 °C in PBS and dialyzed using 300 KDa MWCO membrane (Spectra/Por Float-A-Lyzer G2) in sodium carbonate buffer following the manufacturer's instructions. Virus-like particles

were subsequently incubated with AF-555 NHS ester for 1 h at 25 °C and dialyzed using 300 KDa MWCO membrane in PBS for 2 days. Mice were immunized with a dose containing 1 μg YU-gp120 protein in 100 μl of PBS in the flanks.

YU-gp120-SpyTag HIV envelope production

A SpyTag sequence was inserted in the N-terminal part of the YU-gp120 sequence. The recombinant protein was produced in 293F cells transfected with YU-gp120-SpyTag expressing pcDNA3.1 plasmid (a kind gift from B. Haynes) as described⁴². Briefly, cell supernatant was filtered with 0.8 μm filter, mixed with *Galanthus nivalis* lectin (GNL) binding buffer and loaded onto GNL-agarose column previously equilibrated with GNL binding buffer (five times the volume). After that, the column was washed five times with GNL binding buffer and the protein was eluted using a Mannose solution. The purity was assessed by running an SDS-PAGE.

CR2-C3dg binding measurement

The on- and off-rate and the equilibrium dissociation constant for the CR2 interaction with C3dg was measured using Bio-Layer interferometry (Octet, Sartorius). We loaded a His-tagged human CR2 protein (Bio-technne) to Nickel-NTA sensor at a concentration of 36.8 nM. Human C3dg protein was produced as described⁵³. Briefly, human C3dg cDNA containing the Cys1010Ala mutation inserted into pET13b expression plasmid lacking the His-tag (a kind gift from J. Eisenman) was transformed into BL21 *Escherichia coli*. After induction with IPTG, soluble C3dg was purified from bacterial lysates using CM Sepharose followed by gel filtration on a Superdex 200 column. Association of the C3dg protein with CR2 was measured for concentrations ranging from 0.023 μM to 2.9 μM . The equilibrium dissociation constant was determined by fitting the plateau values with a binding model, yielding $K_D = 317 \pm 30$ nM. The association and dissociation rates were determined by fitting a kinetic model yielding $k_{on} = 616,154 \text{ M}^{-1} \text{ s}^{-1}$, $k_{off} = 0.15 \text{ s}^{-1}$.

IC-FDC dissociation mathematical model

To describe the dynamics of IC dissociation from FDCs at varying CR2 concentrations, we generated a stochastic framework comprising microscopic events that alter the probability of IC survival over time. Specifically, as an IC is loaded onto the FDC membrane, a multiplicity of adhesive bonds forms between the C3d ligands coating the IC particle and the surface CR2. Individual dissociated CR2–C3d pairs can rebind, as long as some bonds remain to hold the IC. Once all bonds open, the IC is irreversibly lost.

Mathematically, starting from maximum bond formation between the IC and CR2 on the corresponding membrane patch (assuming that each membrane patch can host at most one IC), stochastic ICloss proceeds through a one-step master equation:

$$\frac{dP_m}{dt} = r(m+1)P_{m+1}(t) + g(m-1)P_{m-1}(t) - (r(m) + g(m))P_m(t).$$

Here, $P_m(t)$ represents the probability that m bonds remain closed between an IC and the FDC at time t , which evolves due to dissociation of any closed bond at an unbinding rate $r(m) = mk_{off}$ and formation of a new bond at a rebinding rate $g(m) = C(m)k_{on}$. We set $g(0) = 0$ to avoid IC reassociation. Rebinding shifts the equilibrium state away from complete dissociation, stabilizing multivalent binding (IC survival) in the presence of noise. Eventually, all bonds break if one waits long enough. The CR2–C3d single-bond dissociation rate, k_{off} , was obtained from Bio-Layer Interferometry. In the model $k_{off}^{-1} = 1/(0.15 \text{ s}^{-1}) \approx 7 \text{ s}$ sets the time unit. k_{on} was adjusted to recapitulate the typical half-life of ICs observed at known CR2 concentrations.

The key quantity in the rebinding rate, $C(m)$, counts the number of binding configurations (bond arrangements) given m closed bonds.

Importantly, the form of $C(m)$ depends on bond properties (for example, length and flexibility) and binding geometry (for example, C3d spacing, curvature of the IC surface, distance of IC from the FDC surface when bound). We used the all-to-all binding scenario: $C(m) = (n_R - m)(n_L - m)$, whereby each of n_L C3d ligands on a guest IC is accessible to all n_R CR2 on the host membrane patch. This scenario is appropriate for long, flexible molecules like CR2. Note that $C(m)$ changes rapidly with the valency m due to nonlinearity, resulting in a high sensitivity of IC survival to CR2 concentration.

We simulated the model and computed the time-dependent survival probability of an IC, $S(t) = \sum_{m=1}^{\min(n_R, n_L)} P_m(t)$, for a given CR2 concentration (n_R). To account for variations of CR2 density for a given mean value (corresponding to different FDC populations), we consider a Poisson distribution of CR2 level among membrane patches for a certain mean CR2 density $\langle n_R \rangle$: $P(n_R) = e^{-\langle n_R \rangle} \langle n_R \rangle^{n_R} / n_R!$. By averaging over this distribution, we obtain the mean IC survival rate $\langle S(t) \rangle$ and use $\langle S(t) \rangle \langle n_R \rangle$ to represent the overall surface concentration of IC on the FDCs. In Fig. 6b we plot this quantity against time and also extract the half-life (time taken to reach half of the initial IC level) at varying CR2 concentrations.

Anti-CD40L treated mice

Mice were immunized with a first antigen immunocomplex (immunization protocol) and 5 days later injected i.p. with 200 µg anti-CD40L blocking antibody or its isotype control (BioXCell) on the subsequent 2 days. Mice were subsequently immunized with a second antigen immunocomplex and injected again 2 days later with 200 µg anti-CD40L blocking antibody or its isotype control for the subsequent 2 days. Draining LNs were used for flow cytometry and microscopy.

Anti-CD21/35 blocking antibody treated mice

Mice were injected with 2 µg anti-CD21/35-BV421 (clone 7G6; BD Biosciences) subcutaneously in the upper and lower flank to target the brachial, axillary and inguinal draining LNs starting on the day of the experiment and every 2 days thereafter up to three injections. Mice were subsequently immunized with antigen-immunocomplexes (following the immunization protocol described above) and analyzed after 24 h, 4 days and 7 days postimmunization.

ELISA

In immunized mice, sera were obtained at 21 and 56 days after immunization. Plate-bound NP(7)-BSA and NP(25)-BSA (10 µg ml⁻¹) was used to measure antigen-specific antibodies. Class-switched serum immunoglobulin levels were detected using SBA Clonotyping System HRP kit (Southern Biotech). Antibody titers are given as $-\log_2(\text{dilution}) \times 40$. Positive values were defined as those 3 s.d. above mean values of the negative controls⁶.

Quantification and statistical analysis

Prism v.9.1.2 (GraphPad Software) was used to assess statistical significance of non-RNA-seq data. The sample size (n), statistical significance and statistical tests are indicated in the legends. Data distribution was assumed to be normal, but this was not formally tested. Data collection and analysis were not performed blind to the conditions of the experiments and no formal randomization was used. No statistical methods were used to predetermine sample sizes but our sample sizes are similar to those reported in previous publications⁶. All data points were analyzed unless there were technical errors.

Reporting summary

Further information on research design is available in the Nature Portfolio Reporting Summary linked to this article.

Data availability

Ensembl GRCm38 was used as the reference genome to build the index. The mouse scRNASeq data are available in GEO under accession no [GSE213254](https://www.ncbi.nlm.nih.gov/geo/record/GSE213254). Source data are provided with this paper.

Code availability

Matlab script for FDC segmentation is available at <https://github.com/polar/FDCsegmentation>. Code used to analyze scRNASeq is available at https://github.com/FrancisCrickInstitute/Cxcl13_project.

References

58. Messal, H. A. et al. Antigen retrieval and clearing for whole-organ immunofluorescence by FLASH. *Nat. Protoc.* **16**, 239–262 (2021).
59. Butler, A., Hoffman, P., Smibert, P., Papalexis, E. & Satija, R. Integrating single-cell transcriptomic data across different conditions, technologies, and species. *Nat. Biotechnol.* **36**, 411–420 (2018).
60. Li, Y., Liu, P. C., Shen, Y., Snavely, M. D. & Hiraga, K. A cell-based internalization and degradation assay with an activatable fluorescence-quencher probe as a tool for functional antibody screening. *J. Biomol. Screen.* **20**, 869–875 (2015).
61. Bruun, T. U. J., Andersson, A.-M. C., Draper, S. J. & Howarth, M. Engineering a rugged nanoscaffold to enhance plug-and-display vaccination. *ACS Nano* **12**, 8855–8866 (2018).
62. Liao, H.-X. et al. Co-evolution of a broadly neutralizing HIV-1 antibody and founder virus. *Nature* **496**, 469–476 (2013).
63. Nagar, B., Jones, R. G., Diefenbach, R. J., Isenman, D. E. & Rini, J. M. X-ray crystal structure of C3d: a C3 fragment and ligand for complement receptor 2. *Science* **280**, 1277–1281 (1998).

Acknowledgements

We thank D. Calado for the Cr2-KO ($Cr2^{tm1Hmo}$) mice and B. Haynes for the YU-gp120 pcDNA3.1 plasmid. We thank M. Howarth for the SpyTag plasmids and J. Eisenman for the C3dg pET13b plasmid. We thank L. Wasim and S. Hernández for critical reading of the paper. This work was supported by the Francis Crick Institute, which receives its core funding from Cancer Research UK (CC2006), the UK Medical Research Council (CC2006) and the Wellcome Trust (CC2006), and by the UK Medical Research Council (grant MR/X009254/1). S.W. is supported by the National Science Foundation (NSF) Grant MCB-2225947 and an NSF CAREER Award PHY-2146581. For the purpose of open access, the author has applied a CC BY public copyright license to any author accepted manuscript version arising from this submission. We thank the Francis Crick Institute Animal facility, Light Microscopy, Flow Cytometry and Advanced Sequencing Technology Platforms.

Author contributions

A.M.-R. designed and performed the experiments and analyzed the data. S.W. developed and analyzed the mathematical model of IC-FDC dissociation. S.B. analyzed the scRNASeq data. S.M. measured the CR2-C3dg binding rates. A.C. produced the YU-gp120-SpyTag protein. K.M.S. provided advice. B.L. provided the CXCL13-TdTomato mice and advice. P.T. designed the experiments and supervised the research. A.M.-R. and P.T. prepared the paper.

Competing interests

The authors declare no competing interests.

Additional information

Extended data is available for this paper at <https://doi.org/10.1038/s41590-023-01559-1>.

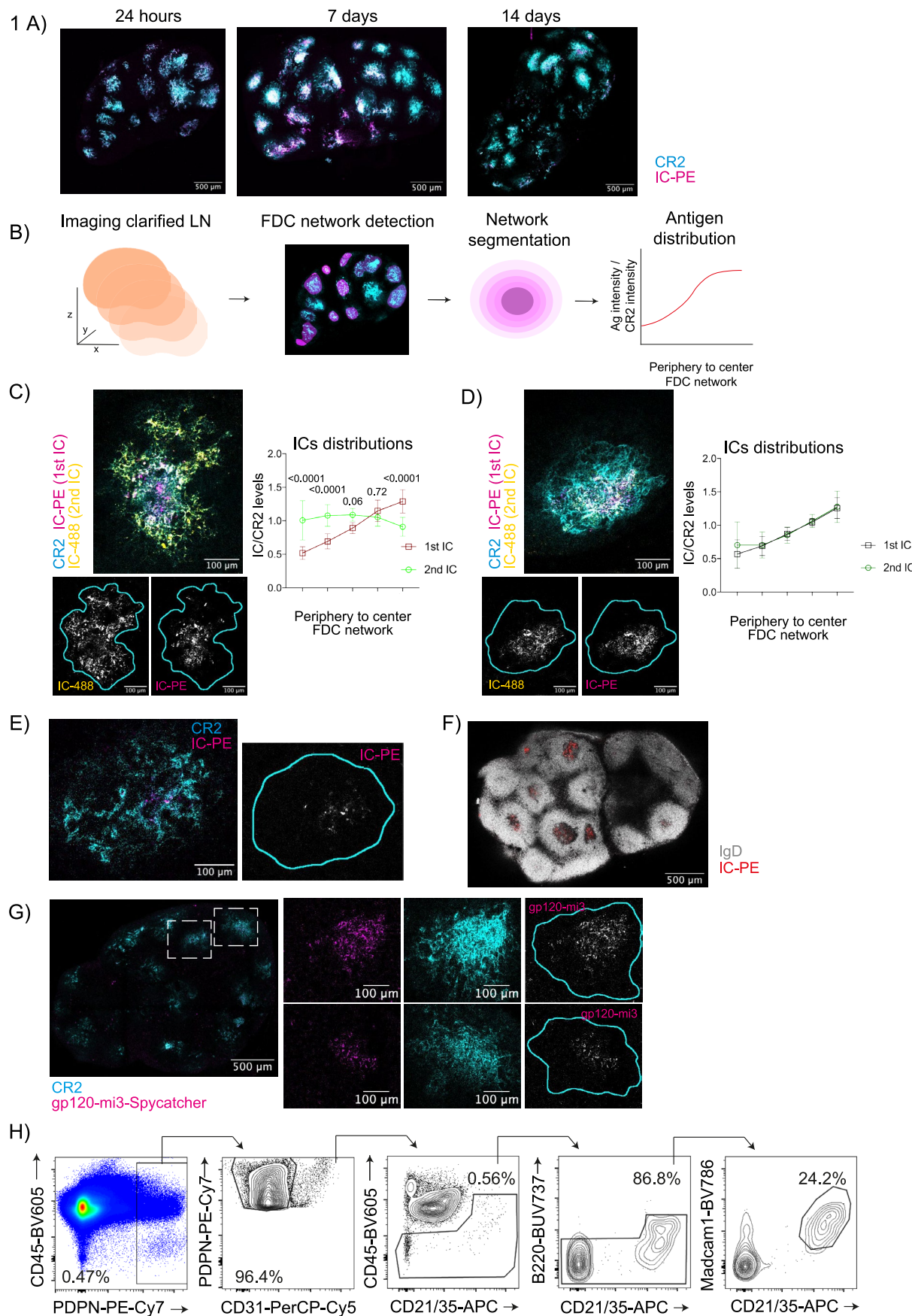
Supplementary information The online version contains supplementary material available at <https://doi.org/10.1038/s41590-023-01559-1>.

Correspondence and requests for materials should be addressed to Pavel Tolar.

Peer review information *Nature Immunology* thanks Michael Carroll and the other, anonymous, reviewer(s) for their contribution to the peer review of this work. Peer review reports are available.

Primary Handling Editor: L. A. Dempsey in collaboration with the *Nature Immunology* team. Peer review reports are available.

Reprints and permissions information is available at www.nature.com/reprints.

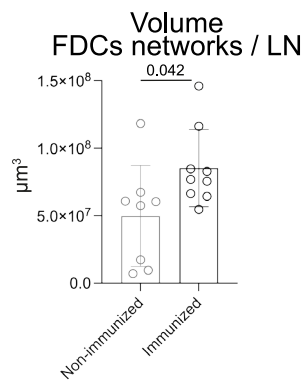


Extended Data Fig. 1 | See next page for caption.

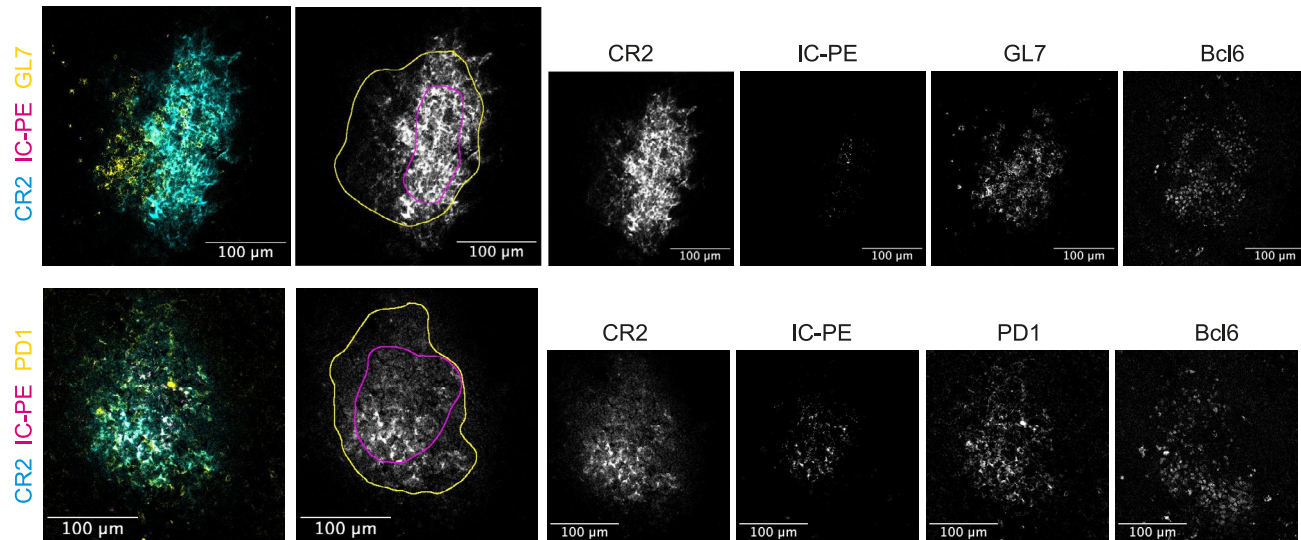
Extended Data Fig. 1 | Antigens centralize on the FDC network. **a**) Maximum intensity projection of confocal images of clarified LNs of mice immunized with IC-PE (magenta). FDC networks are in cyan (anti-CD21/35) ($n = 6$ LNs; 3 experiments). **b**) Image analysis to quantify antigen distribution within each B cell follicle. **c**) Confocal image of an FDC network (cyan) after immunization with two subsequent ICs in PBS analyzed 7 days after the first immunization (IC-PE; magenta) and 24 hours after the second (IC-488; yellow). Single-color images of IC-488 (left) and IC-PE (right) are shown below. Cyan line demarcates FDC network boundary based on anti-CD21/35 staining. Right, quantification of the distribution of both antigens on the FDC network. ($n = 8$ LNs; 2 experiments). **d**) Confocal image of an FDC network (cyan) after immunization with two subsequent ICs as in C for 14 and 7 days. Single-color images of IC-488 (left) and IC-PE (right) are shown below. Cyan line demarcates the FDC network boundary based on anti-CD21/35 staining. Right, quantification of the distribution of

both antigens on the FDC network ($n = 12$ LNs; 2 experiments). **e**) Image of an LN FDC network (cyan) 56 days after immunization with IC-PE (magenta). Right, single-color image of IC-PE (gray) with cyan line demarcating the FDC network boundary based on anti-CD21/35 staining ($n = 4$ LNs; 1 experiment). **f**) Image of a draining LN 21 days after immunization with IC-PE (red). Naïve B cells are shown in gray (anti-IgD). ($n = 4$ LNs; 2 experiments). **g**) Image of a draining LN 7 days after immunization with AF555-labeled mi3-Spycatcher nanoparticles coated with YU-gp120-Spytag HIV envelope protein (magenta). FDC networks are shown in cyan (anti-CD21/35). White square indicates the region magnified. Cyan line demarcating the FDC network boundary based on anti-CD21/35 staining ($n = 3$ LNs; 2 experiments). **h**) Flow cytometry gating strategy to analyze FDCs. Quantitative data show the mean \pm SD analysis by two-tailed t-test or one-way ANOVA with multiple comparisons.

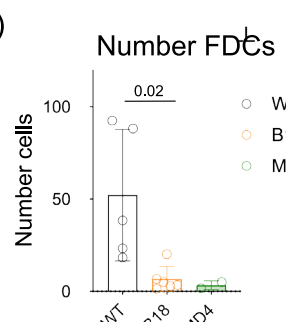
A)



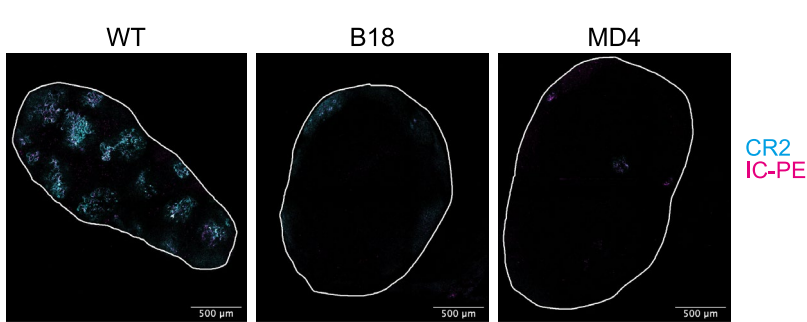
B)



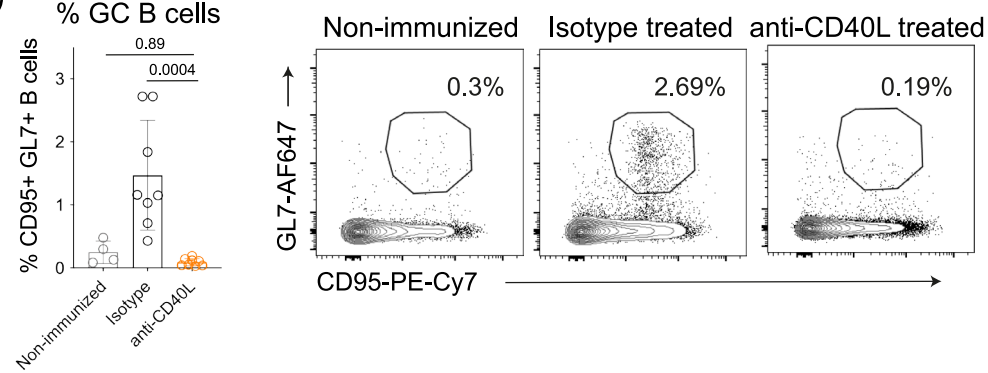
C)



D)



E)

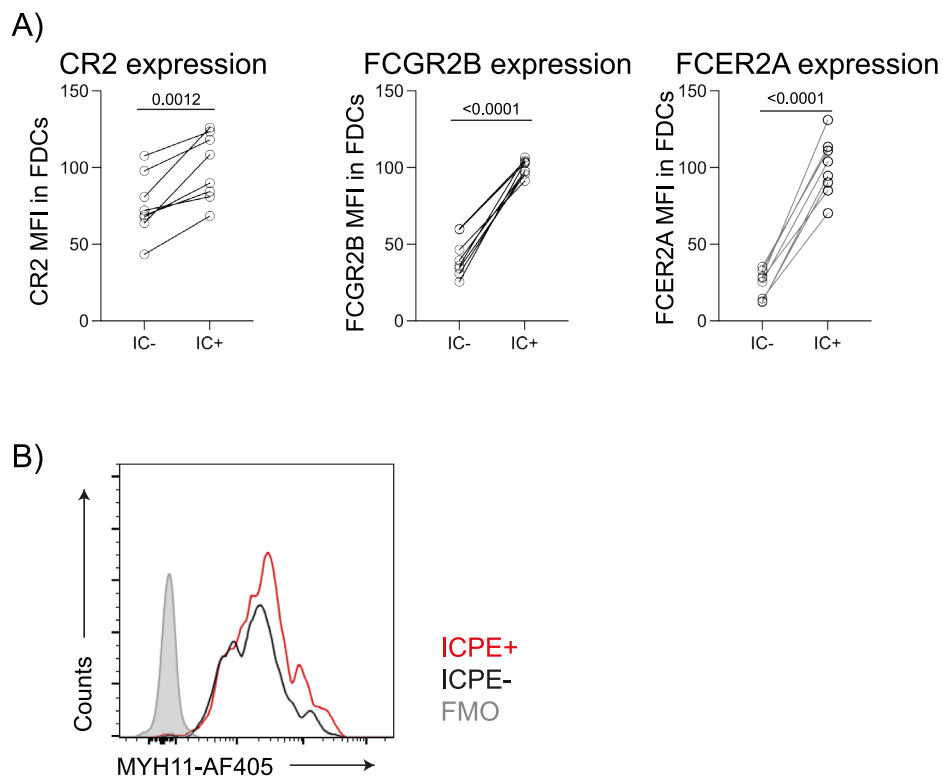


Extended Data Fig. 2 | See next page for caption.

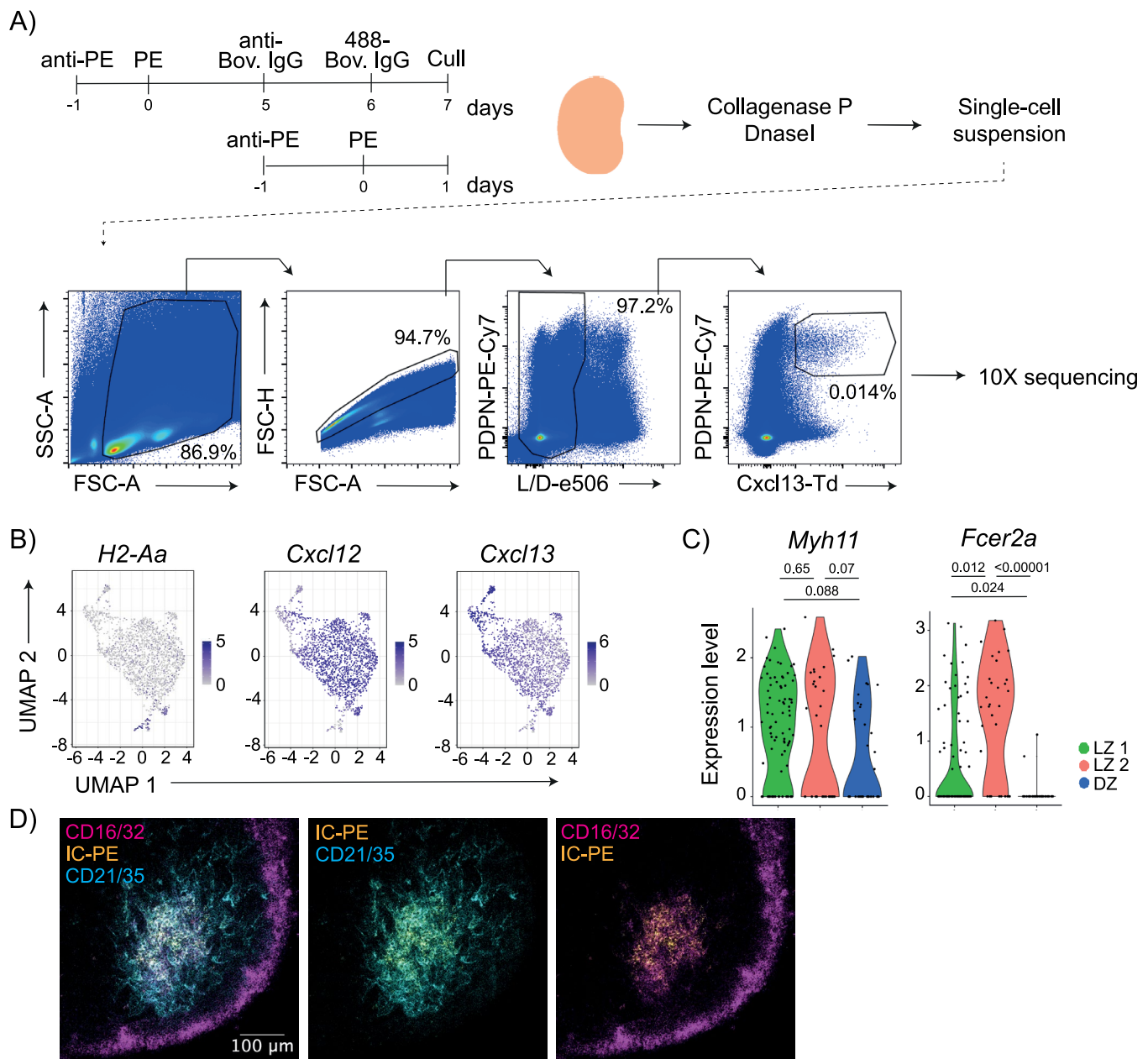
Extended Data Fig. 2 | B cell activation is required for FDC expansion.

a) Quantification of the FDC network volume per LN based on anti-CD21/35 staining in clarified LNs from non-immunized ($n = 8$ mice) and 13 days post-immunized ($n = 9$) mice with IC-PE. **b)** Representative immunofluorescence images of LN B cell GCs from mice immunized for 14 days with IC-PE. Upper row shows the merged image of GL7 (yellow), IC-PE (magenta), and anti-CD21/35 (cyan) and the corresponding single-color images (gray). Yellow line demarcates GL7 staining and magenta line IC-PE localization ($n = 4$ mice). Lower row shows the merged image of anti-PD1 (yellow), IC-PE (magenta) and anti-CD21/35 (cyan) and the corresponding single-color images (gray). Yellow line demarcates PD1

staining and magenta line IC-PE localization ($n = 4$ mice). **c)** FDC numbers in non-transgenic C57BL/6 (WT; $n = 5$) and BCR-transgenic B1-8f (B1-8^{flx} Igκ^{-/-}; $n = 6$) and MD4 mice ($n = 2$) 24 hours after immunization with IC-PE. **d)** Representative confocal images of LNs from non-tg (WT), B1-8f and MD4 mice 24 hours after immunization with IC-PE (magenta). FDC networks are shown in cyan (anti-CD21/35). The white line delimits the edges of the organs. **e)** Percentage of GCB cells in non-immunized (light gray; $n = 4$ mice) and IC-immunized mice treated with anti-CD40L (orange; $n = 8$ mice) or isotype control antibody (black; $n = 8$ mice) as described in Fig. 2b. Quantitative data show means \pm SD and analysis by two-tailed one-way ANOVA with multiple comparisons.



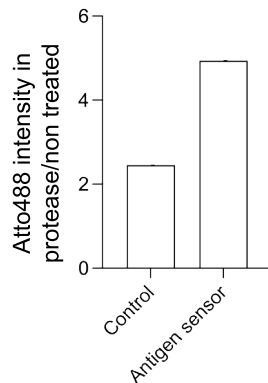
Extended Data Fig. 3 | IC-binding receptor expression on FDCs. **a**) CR2, FCGR2B and FCER2A membrane expression on IC⁺ and IC⁻ FDCs 7 days after immunization (n = 7 mice; 2 experiments). **b**) Histogram showing Myosin heavy chain 11 (MYH11) expression in IC-PE⁺ and IC-PE⁻ FDCs 7 days after immunization. Quantitative data show means ± SD and analysis by two-tailed paired t-test.



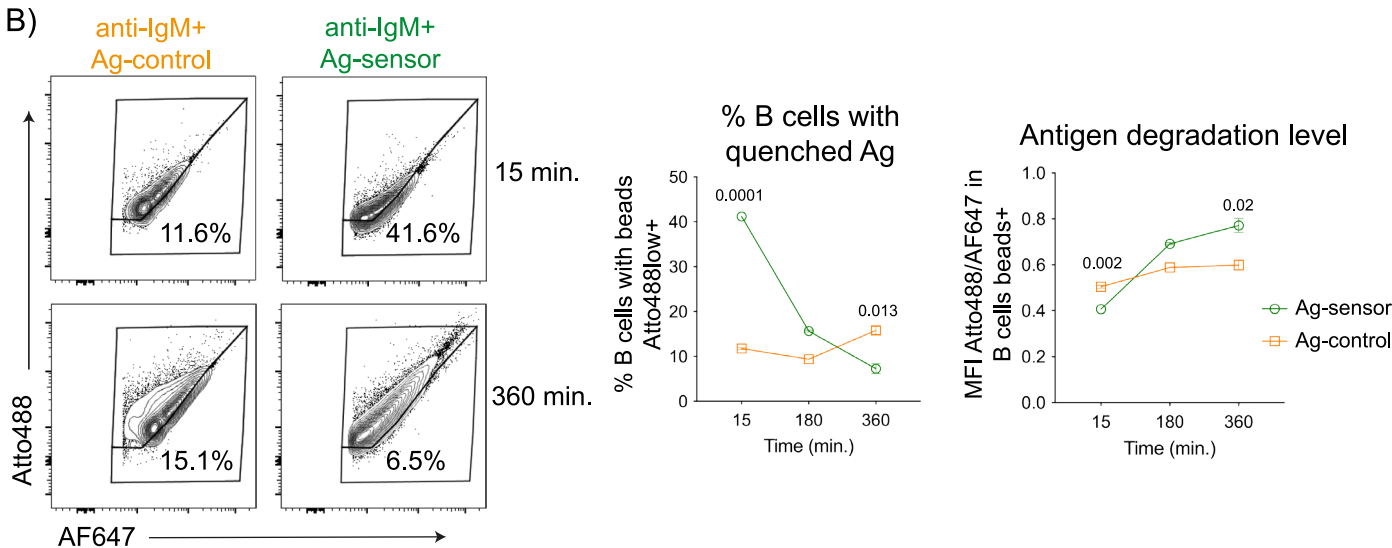
Extended Data Fig. 4 | ScRNAseq of follicular stromal cells. **a)** Experimental workflow for scRNAseq of Cxcl13-TdTomato⁺ LN cells. Cxcl13-TdTomato mice were immunized consecutively with two ICs separated by 7 days or only with one IC. 24 h after the last immunization, draining LNs were dissociated into a single-cell suspension, stained and live cells were flow-sorted based on PDPN and TdTomato positivity. Single-sorted cells were used for 10x RNA sequencing. **b)** Feature plots showing expression of markers for hematopoietic cells (*H2-*

Aa) and cytokines important for LN organization, *Cxcl12* and *Cxcl13*. **c)** Violin plots showing the expression of *Myh11* and *Fcer2a* on the three FDC clusters from Fig. 4c (LZ 1 in green, LZ 2 in red, and DZ in blue). One-tail adjusted P for multiple comparisons. **d)** Confocal image of a LN from a mouse after 7 days postimmunization with IC-PE (yellow). CR2 staining is shown in cyan and CD16/32 in magenta (n = 4 LNs; 2 experiments).

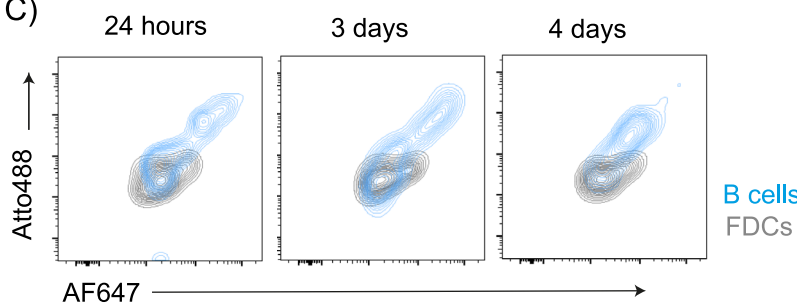
A) Atto488 signal after protease treatment



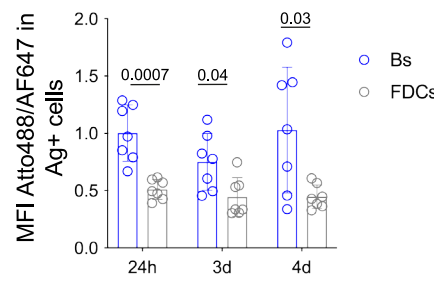
B)



C)

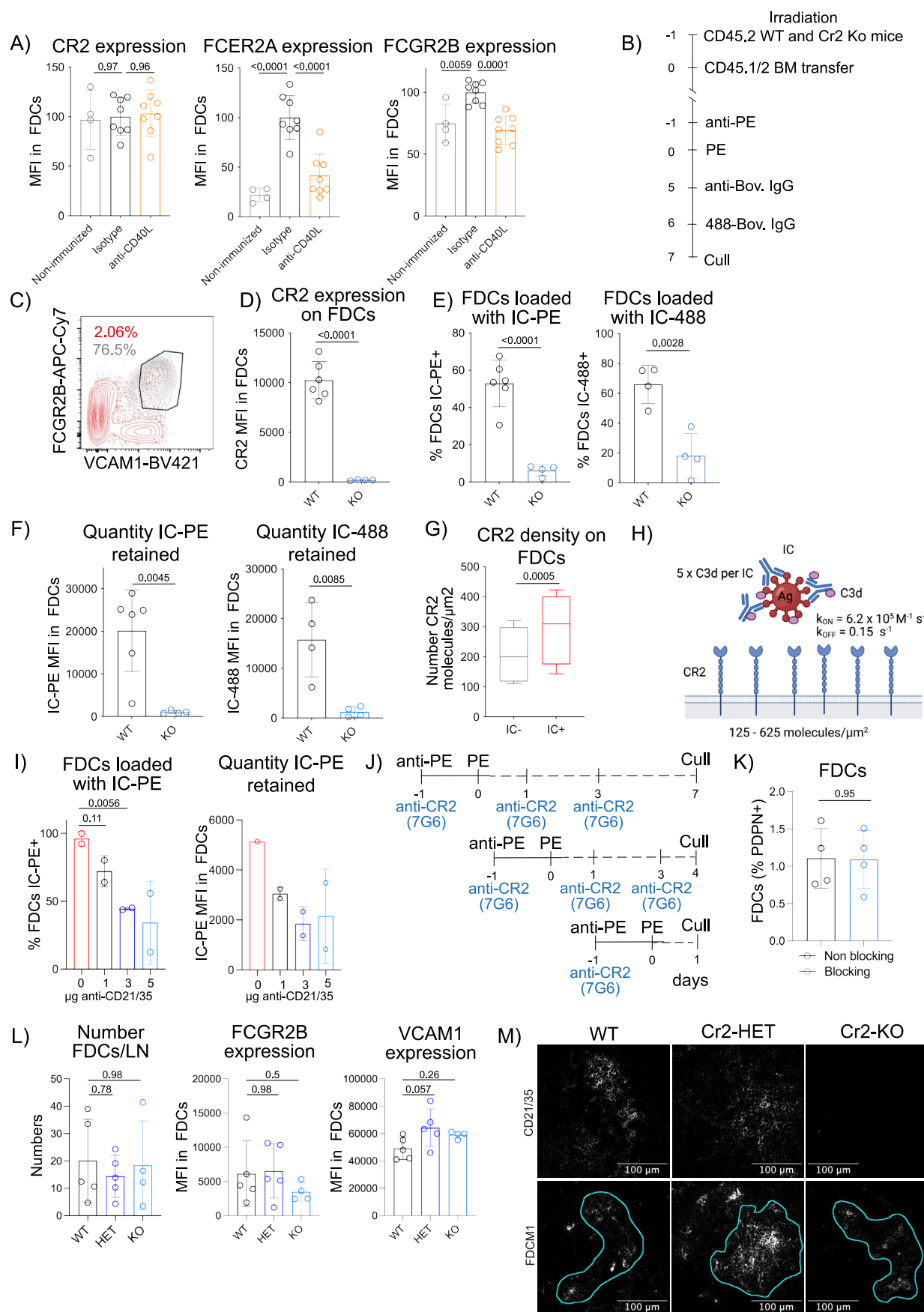


D) Antigen degradation level



Extended Data Fig. 5 | Antigen degradation by FDCs. **a)** Quantification of Atto488 intensity after treating the control sensor lacking the BHQ-1 quencher or antigen-degradation sensor (1:9 antigen:quencher molar ratio) with protease for 30 min at 37 °C. **b)** Naïve B cells were incubated with beads coated with anti-IgM and the antigen-degradation sensor (green) or control sensor (orange) at indicated times at 37 °C. Plots illustrate Atto488 and AF647 intensity on B cells containing degradation sensor beads or control sensor beads. Graphs show the percentage of B cells containing quenched antigen (% of Atto488-low) and the

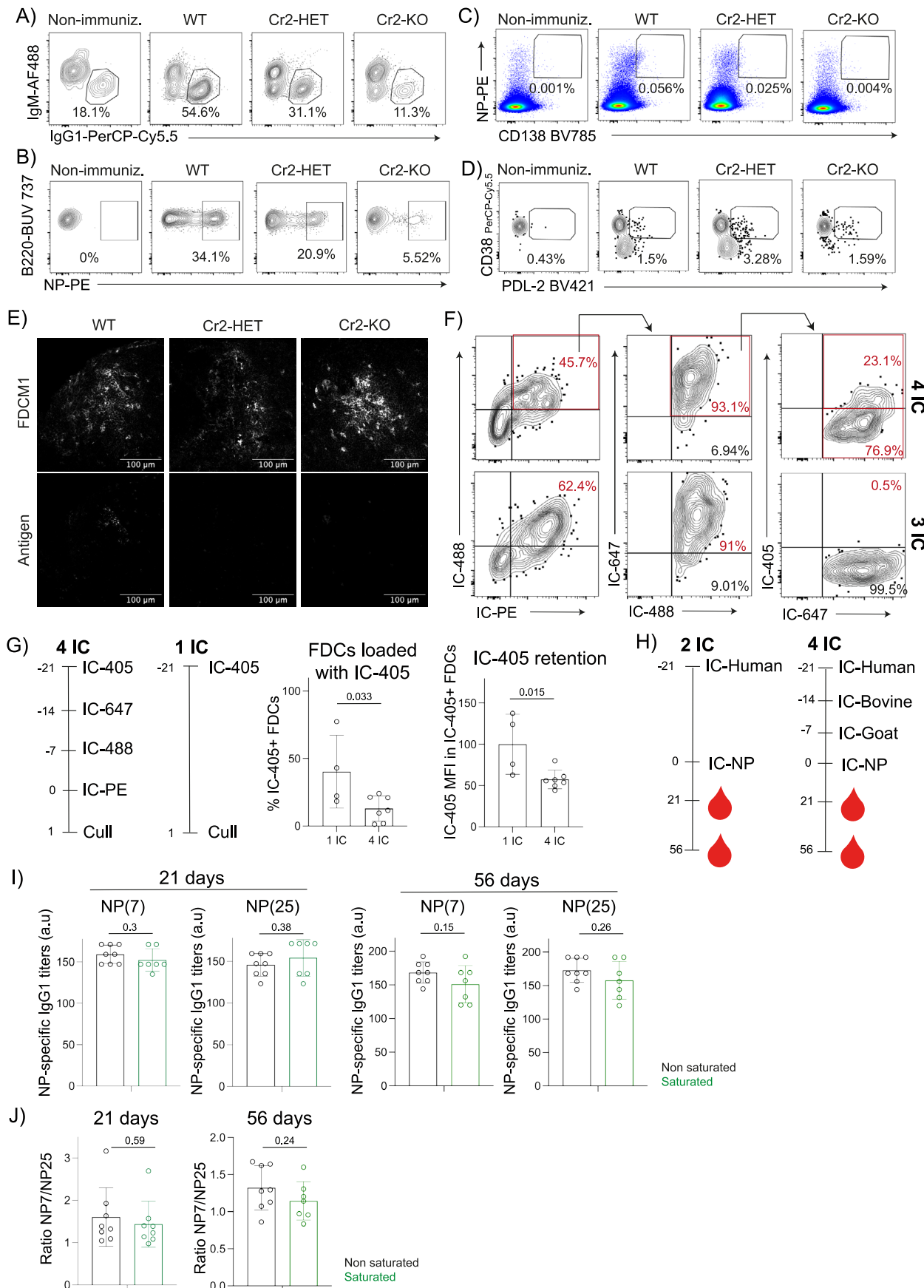
levels of antigen degradation on B cells containing beads (measured as Atto488/AF647 intensity ratio) (2 experiments). **c)** Contour plots show Atto488 and AF647 levels on B cells (blue) and FDCs (gray) containing IC-antigen-degradation sensor at different time points post-immunization. **d)** Quantification of the antigen degradation levels in antigen⁺ B cells and FDCs at different time points post-immunization. (n = 7 mice; 2 experiments). All quantitative data show means ± SD analyzed by two-tailed unpaired t-test.



Extended Data Fig. 6 | See next page for caption.

Extended Data Fig. 6 | *In vivo* IC deposition on FDCs requires CR2 expression. **a**) CR2, FCER2A and FCGR2B membrane expression on FDCs from mice described in Fig. 2c. **b**) Experimental workflow. Lethally irradiated CD45.2 WT (n = 6) and *Cr2*-KO (n = 4) mice reconstituted with bone marrow cells from WT CD45.1/CD45.2 mice and immunized with IC-PE and IC-488 6 days later. **c**) Gating strategy based on FCGR2B and VCAM1 expression to analyze FDCs in CD45.2 WT and *Cr2*-KO mice reconstituted with WT CD45.1/CD45.2 BM. In gray, FCGR2B and VCAM1 expression on WT FDCs (PDPN⁺ CD31⁺ Madcam1⁺ CD21/35^{hi}); in red, on PDPN⁺ CD31⁻ stromal cells. **d**) CR2 expression on WT and *Cr2*-KO FDCs from mice as described in (B). **e**) Percentage of FDCs loaded with IC-PE and IC-488 from mice described in (B). **f**) Quantity of IC loaded in the FDC network from mice described in (B). **g**) Surface CR2 density on IC⁺ (red) or IC⁻ (gray) FDCs 7 days after immunization. Plots show the median (line), the 25th and 75th percentiles (box) and 1.5x the interquartile range (whiskers) of the number of CR2 molecules/

μm² (n = 8 mice; 2 experiments). **h**) Schematic of the binding of a C3d-coated IC to the surface of an FDC illustrating the mathematical modelling parameters. **i**) Percentage of FDCs loaded with IC-PE and amount of IC-PE 24 h after IC-PE immunization and injection of anti-CD21/35 blocking antibody (n = 2 mice). **j**) Immunization workflow to analyze the effect of blocking CR2-C3d binding using an anti-CD21/35 antibody (7G6). **k**) Percentage of FDCs within the stromal PDPN⁺ cells in LNs from mice untreated (black) or treated (blue) for 7 days with anti-CD21/35 (7G6) blocking antibody as shown in J (n = 4 mice). **l**) Number of FDCs per LN and expression of FCGR2B and VCAM1 in WT (black; n = 5), *Cr2*-HET (dark blue; n = 5) and *Cr2*-KO mice (light blue; n = 4) bone-marrow reconstituted with WT CD45.1 cells. **m**) Representative images of a FDC network from mice described in L. Cyan line demarcates FDC network based on FDCM1 stain (n = 5 mice; 2 experiments). Quantitative data show means ± SD and analysis by two-tailed unpaired t-test or One-way ANOVA with multiple comparisons.



Extended Data Fig. 7 | See next page for caption.

Extended Data Fig. 7 | Central FDCs can get partially saturated. **a**) Gating strategy to analyze IgG1⁺ cells within GC CD45.1⁺ donor B cells in WT, Cr2-HET and Cr2-KO mice bone-marrow reconstituted with CD45.1⁺ WT cells and immunized for 21 days with IC-NP. Non-immunized mice shown as control. **b**) Gating strategy to analyze NP-specific B cells within GC CD45.1⁺ donor B cells from mice described in A. **c**) Gating strategy to analyze plasmablasts (CD138⁺ NP⁺ within CD45.1^{+/−}) from mice described in A. **d**) Gating strategy to analyze memory B cells (CD38^{hi} PDL-2⁺ within the NP-specific CD45.1⁺ donor cells) from mice described in A. **e**) Representative confocal images of FDC networks from LNs of WT, Cr2-HET and Cr2-KO mice bone-marrow reconstituted with WT CD45.1 cells and immunized for 21 days with IC NP-PE (n = 3 mice). Upper panel shows FDCM1 staining. Lower panel shows NP-PE. **f**) Gating strategy to analyze FDCs containing different combinations of ICs from consecutive immunizations with three (lower panel) or four (upper panel) different fluorescent antigen-ICs as indicated

in Fig. 7a, b, g.) Workflow to analyze antigen displacement by subsequent immunizations. Mice were immunized with IC-405 alone or followed by four subsequent immunizations with different ICs. Graphs show the percentage of FDCs loaded with the first antigen and the quantity (MFI) of the loaded antigen in the two groups of mice (n = 7 mice). **h**) Immunization workflow to analyze the antigen-specific antibody response generated to NP under non-saturating (2-IC) or saturating conditions (4-IC). **i**) Titers of high-affinity (NP(7)-BSA) and total (NP(25)-BSA) NP-specific IgG1 in sera of mice 21 and 56 days after immunization with either two antigen-ICs (No saturation condition; black; n = 8 mice) or four antigen-ICs (Saturation condition; green; n = 7 mice) as in D. **j**) Ratio of binding to NP(7) and NP(25), as measured by ELISA in mice immunized as in I. Quantitative data show means ± SD and analysis by two-tailed unpaired t-test with multiple comparisons.

Reporting Summary

Nature Portfolio wishes to improve the reproducibility of the work that we publish. This form provides structure for consistency and transparency in reporting. For further information on Nature Portfolio policies, see our [Editorial Policies](#) and the [Editorial Policy Checklist](#).

Statistics

For all statistical analyses, confirm that the following items are present in the figure legend, table legend, main text, or Methods section.

n/a Confirmed

- The exact sample size (n) for each experimental group/condition, given as a discrete number and unit of measurement
- A statement on whether measurements were taken from distinct samples or whether the same sample was measured repeatedly
- The statistical test(s) used AND whether they are one- or two-sided
Only common tests should be described solely by name; describe more complex techniques in the Methods section.
- A description of all covariates tested
- A description of any assumptions or corrections, such as tests of normality and adjustment for multiple comparisons
- A full description of the statistical parameters including central tendency (e.g. means) or other basic estimates (e.g. regression coefficient) AND variation (e.g. standard deviation) or associated estimates of uncertainty (e.g. confidence intervals)
- For null hypothesis testing, the test statistic (e.g. F , t , r) with confidence intervals, effect sizes, degrees of freedom and P value noted
Give P values as exact values whenever suitable.
- For Bayesian analysis, information on the choice of priors and Markov chain Monte Carlo settings
- For hierarchical and complex designs, identification of the appropriate level for tests and full reporting of outcomes
- Estimates of effect sizes (e.g. Cohen's d , Pearson's r), indicating how they were calculated

Our web collection on [statistics for biologists](#) contains articles on many of the points above.

Software and code

Policy information about [availability of computer code](#)

Data collection FACSDiva (BD Biosciences, v8.0.1), Leica (LAS AF and LAS X)

Data analysis Seurat R (v 3.1.5), Matlab (R2018b), FIJI ImageJ2 (v 2.3.0/1.53q), R Studio (2021.09.1), Prism (GraphPad v9), ImageJ (2.0.0-rc-43/1.53g), FlowJo(v10), Imaris 9.5.1, BioRender, CellRanger pipeline version 3.

For manuscripts utilizing custom algorithms or software that are central to the research but not yet described in published literature, software must be made available to editors and reviewers. We strongly encourage code deposition in a community repository (e.g. GitHub). See the Nature Portfolio [guidelines for submitting code & software](#) for further information.

Data

Policy information about [availability of data](#)

All manuscripts must include a [data availability statement](#). This statement should provide the following information, where applicable:

- Accession codes, unique identifiers, or web links for publicly available datasets
- A description of any restrictions on data availability
- For clinical datasets or third party data, please ensure that the statement adheres to our [policy](#)

Data availability

Source data are provided with this manuscript

Human research participants

Policy information about [studies involving human research participants and Sex and Gender in Research](#).

Reporting on sex and gender

N/A

Population characteristics

N/A

Recruitment

N/A

Ethics oversight

N/A

Note that full information on the approval of the study protocol must also be provided in the manuscript.

Field-specific reporting

Please select the one below that is the best fit for your research. If you are not sure, read the appropriate sections before making your selection.

Life sciences Behavioural & social sciences Ecological, evolutionary & environmental sciences

For a reference copy of the document with all sections, see nature.com/documents/nr-reporting-summary-flat.pdf

Life sciences study design

All studies must disclose on these points even when the disclosure is negative.

Sample size No statistical methods were used to pre-determine sample sizes but our sample sizes are similar to those reported in previous publications

Data exclusions Pre-established exclusion of organs from mice where no fluorescent antigen was detected on the LNs after being immunized, indicating that the immunization protocol was not properly executed.

Replication Experiments were repeated at least three times and/or with sufficient animals per group to demonstrate statistical significance. All experiments are reproducible.

Randomization No formal randomization was performed

Blinding Blinding was not performed since the data was quantitative and not subjective.

Reporting for specific materials, systems and methods

We require information from authors about some types of materials, experimental systems and methods used in many studies. Here, indicate whether each material, system or method listed is relevant to your study. If you are not sure if a list item applies to your research, read the appropriate section before selecting a response.

Materials & experimental systems

n/a	Involved in the study
<input type="checkbox"/>	<input checked="" type="checkbox"/> Antibodies
<input type="checkbox"/>	<input checked="" type="checkbox"/> Eukaryotic cell lines
<input checked="" type="checkbox"/>	<input type="checkbox"/> Palaeontology and archaeology
<input type="checkbox"/>	<input checked="" type="checkbox"/> Animals and other organisms
<input checked="" type="checkbox"/>	<input type="checkbox"/> Clinical data
<input checked="" type="checkbox"/>	<input type="checkbox"/> Dual use research of concern

Methods

n/a	Involved in the study
<input checked="" type="checkbox"/>	<input type="checkbox"/> ChIP-seq
<input type="checkbox"/>	<input checked="" type="checkbox"/> Flow cytometry
<input checked="" type="checkbox"/>	<input type="checkbox"/> MRI-based neuroimaging

Antibodies

Antibodies used

Antibodies used (Reagent and conjugate, Clone, Cat.No, Source, Dilution):
anti-B220 BV605 (RA3-6B2), 103243, Biolegend (1/200)
anti-B220-BUV737 (RA3-6B2), 612839, BD Biosciences (1/200)
anti-B220-BV421 (RA3-6B2), 103240, Biolegend (1/200)

anti-Bcl6 AF488 (K112-91), 561524, BD Biosciences (1/100)
 anti-CD45.2-BV605 (104), 109841, Biolegend (1/200)
 anti-CD45.2 FITC (104), 11-0454-85, eBIOSCIENCES (1/200)
 anti-PDPN PE-cy7 (8.1.1), 127411, Biolegend (1/300)
 anti-PD1 Biotin (29F.1A12), 135212, Biolegend (1/100)
 anti-PDL2 Bv421 (TY25), 564245, BD Horizon (1/200)
 anti-CD31-PerCP-Cy5 (390), 102420, Biolegend (1/250)
 anti-CD21/35 PE (7E9), 123409, Biolegend (1/200)
 anti-CD21/35 FITC (7E9), 123407, Biolegend (1/200)
 anti-CD21/35 APC (7E9), 123411, Biolegend (1/200 Flow, 1/50 Clarification)
 anti-CD21/35 BV421 (7E9), 123421, Biolegend (1/200)
 anti-CD21/35 BV421 (7G6), 562756, BD Biosciences (1/200)
 anti-CD21/35 APC-Cy7 (7E9), 123417, Biolegend (1/200)
 anti-CD35 BV421 (8C12), 740029, BD Biosciences
 anti-CD35 Biotin (8C12), 553816, BD Pharmigen (1/200)
 anti-CD45.1- BV711 (A20), 110739, Biolegend (1/200)
 anti-CD80 BV650 (16-10A1), 563687, BD Horizon (1/200)
 anti-IgD AF647 (11-23c), 405708, Biolegend (1/200)
 anti-IgM BUV395 (R6-60.2) 564025 BD Biosciences (1/100)
 anti-IgG1 PerCP-Cy5.5 (RMG1-1) 406611 Biolegend (1/200)
 anti-MAdCAM-1 BV786 (MECA-367), 742817, BD Biosciences (1/200)
 anti-T- and B-Cell activation antigen AF647 (GL7), 561529, BD Biosciences (1/200)
 anti-CD95-PEcy7 (Jo2), 557653, BD Pharmigen (1/200)
 anti-CD23-BUV395 (B3B4), 740216, BD Biosciences (1/200)
 anti-CD16/32 purified (2.4G2), 553141, BD Biosciences (1/300)
 anti-CD16/32 APC-cy7 (2.4G2), 101327, Biolegend (1/200)
 anti-CD16/CD32 APC (2.4G2), 558636, BD Biosciences (1/200)
 anti-CD38 PerCP-Cy5.5 (90), 102722, Biolegend (1/200)
 anti-CD138 BV786 (281-2), 142534, Biolegend (1/200)
 anti-H2-Kb/Dd FITC (28-8-6), 114605, Biolegend (1/200)
 anti-PDPN polyclonal, AF3244, R&D (1/50)
 anti-Myh11 (SM-M10), MA5-11971, Thermo Fisher (1/200)
 anti-FDCM1, 551320, BD (1/75)

donkey anti-goat IgG, 705-001-003, Jackson Imm
 goat Fab2 IgG anti-horse, 108-006-003, Jackson Imm
 Goat IgG, 005-000-003, Jackson Imm
 rb anti-human IgG, 309-001-003, Jackson Imm
 Human IgG, 009-000-003, Jackson Imm
 anti-B-Phycoerythrin , 100-4199, Rockland
 anti-bovine IgG, 301-001-003, Jackson Imm
 Bovine IgG, 001-000-003, Jackson Imm
 anti-mouse CD40L (MR-1), BE0017-1, BioXCell
 polyclonal hamster IgG, BE0087, BioXCell

anti-rat IgG AF488, 44165, Cell Signaling (1/300)
 anti-goat AF488, A21222, LIFE TECHNOLOGY (1/300)
 SA BUV737, 612775, BD Biosciences (1/300)
 SA APC, 405207, Biolegend (1/300)

Validation

All antibodies came from commercial vendors, and were validated by the manufacturers on the official website for the species and specified application (Flow cytometry, microscopy)

Eukaryotic cell lines

Policy information about [cell lines and Sex and Gender in Research](#)

Cell line source(s)

293-F Cells

Authentication

Cell line identity was confirmed by STR profiling at The Francis Crick Institute

Mycoplasma contamination

Cells tested negative for mycoplasma contamination

Commonly misidentified lines
(See [ICLAC](#) register)

None

Animals and other research organisms

Policy information about [studies involving animals; ARRIVE guidelines](#) recommended for reporting animal research, and [Sex and Gender in Research](#)

Laboratory animals

C57BL/6, Cr2-KO (Cr2tm1Hmo), CXCL13-TdTomato (Tg(Cxcl13-Cre/tdTomato)719Biat), B1-8fl (Igthm4Cgn IgkCtm1Cgn/tm1Cgn), MD4 (C57BL/6Tg(IghelMD4)4Ccg/J) and CD45.1 (B6.SJL-Ptprca Pepcb /Boyl) mice between 8-12 weeks of age were used. Both males and

females were used and matched between groups.

Wild animals	None
Reporting on sex	This information has not been collected
Field-collected samples	None
Ethics oversight	All experiments were approved by the Francis Crick Institute and UCL Ethical Review Panels and the UK Home Office.

Note that full information on the approval of the study protocol must also be provided in the manuscript.

Flow Cytometry

Plots

Confirm that:

- The axis labels state the marker and fluorochrome used (e.g. CD4-FITC).
- The axis scales are clearly visible. Include numbers along axes only for bottom left plot of group (a 'group' is an analysis of identical markers).
- All plots are contour plots with outliers or pseudocolor plots.
- A numerical value for number of cells or percentage (with statistics) is provided.

Methodology

Sample preparation	A description of the sample preparation is detailed in the methods section
Instrument	LSR-Fortessa, LSR Fortessa Symphony, LSR Fortessa X20
Software	FACSDiva (BD Biosciences, v8.0.1), FlowJO(v10)
Cell population abundance	Cellular population abundance is reported in the manuscript. Post-sorted fractions were directly analysed by scRNAseq, which reported the purity of the sample.
Gating strategy	FDCs gating strategy is reported in the paper. FDCs were gated by FSC/SSC and afterwards by alive cells, excluding hematopoietic cells (CD45+ PDPN-) and specifically B cells (B220+), and selecting those stromal cells (PDPN+), non-endothelial (CD31-), expressing high levels of CR2 (CD21/35hi) and Madcam1+ integrin receptor. Lymphocytes were gated by FSC/SSC and afterwards by alive cells.

Tick this box to confirm that a figure exemplifying the gating strategy is provided in the Supplementary Information.